NTNU – Trondheim
Norwegian University of
Science and Technology

Wetting Properties of Springtail Cuticles: A Quantitative Analysis

Runar Sandnes

Nanotechnology
Submission date: July 2012
Supervisor: Christian Thaulow, IPM

Norwegian University of Science and Technology
Department of Engineering Design and Materials

Wetting Properties of Springtail Cuticles: A Quantitative Analysis

Master's thesis, Norwegian University of Science and Technology (NTNU)

Author: Runar Sandnes

Supervisor: Prof. Christian Thaulow, Department of Engineering Design and Materials, NTNU

July 17, 2012

Abstract

With the prospect of producing superhydrophobic and mechanically stable biomimetic surfaces, the water repellent properties of springtail cuticles are investigated quantitatively. The analysis is based on apparent contact angle measurements on nine springtail species and SEM and AFM images of their cuticles. It is argued that water exists in a metastable Cassie-Baxter state on the cuticle and that three-phase line tension of the order of 10^{-8} J/m contributes to high apparent contact angles. A model is developed to assess the significance of a recently reported re-entrant geometry of the cuticle granules and to study the resistance of the cuticle against wetting. The model estimates that springtails resist wetting under hydrostatic pressures up to $10^4 - 10^5$ Pa, and that re-entrant granule profiles increase the wetting resistance by $50 - 400\%$. To explain the low contact angle hysteresis observed on the cuticles, new equations are proposed to include the effect of three-phase line tension. Again, a line tension magnitude of the order of 10^{-8} J/m can account for the experimental findings. This work indicates that the sub-micron size scale of the springtail cuticle granules provides an elegant approach for achieving water repellent and mechanically stable surfaces. Two springtail species are singled out as especially promising for biomimetic applications.

Sammendrag

Kutikulaet til spretthaler er et lovende material i biomimetisk sammenheng, da det både er vannavstøtende og mekanisk solid. For å forstå mer om hvorfor spretthalene er vannavstøtende, utføres derfor i denne rapporten en kvantitativ analyse av spretthalekutikulaets fuktningsegenskaper. Analysen baserer seg på en serie kontaktvinkelmålinger gjort på ni forskjellige spretthale-arter og på SEM- og AFM-bilder tatt av disse artenes kutikula. Det argumenteres for at vann eksisterer i en metastabil Cassie-Baxter-tilstand på kutikulaet og at tre-fase-linje-spenning i størrelsesordenen 10^{-8} J/m bidrar til de høye kontaktvinklene som observeres. En modell utledes for å evaluere betydningen av en nylig rapportert overhengende profil på kutikulaenes granuler. Denne modellen benyttes også til å studere hvor stort hydrostatisk trykk som skal til før kutikulaene fuktes. Det estimeres at kutikulaene tåler hydrostatiske trykk opp mot $10^4 - 10^5$ Pa uten at de fuktes, og at en overhengende profil på kutikulaenes granuler øker fuktningsmotstanden med $50 - 400\%$. For å forklare den lave kontaktvinkelhysteresen som observeres på spretthalenes kutikula, framsettes nye ligninger som tar høyde for effekten av tre-fase-linje-spenning. Igjen gir en tre-fase-linje-spenning i størrelsesordenen 10^{-8} J/m et godt samsvar mellom teori og observasjon. Denne rapporten tyder på at størrelsen til spretthalekutikulaenes granuler, hvilket er i området sub-mikrometer, utgjør en elegant strategi for å oppnå vannavstøtende og mekanisk solide overflater. To spretthalearter utpekes som spesielt lovende for biomimetiske anvendelser.

Acknowledgements

First of all, I wish to thank Prof. Christian Thaulow for giving me the opportunity to write a thesis about a topic that I find intriguing. His enthusiasm, optimism and broad field of interest provide an atmosphere in which it is a pleasure to write a master's thesis.

I am also especially thankful to PhD candidate Håkon A. Holm Gundersen, for many reasons. All along my thesis work he has given me invaluable feedback, new perspectives and suggestions for relevant literature. In addition, by bringing about high-resolution SEM and AFM images and conducting contact angle measurements on nine springtail species, he has performed the experimental work that made the quantitative analysis in this thesis possible. I would also like to thank Kristin Fjellvang for her important experimental discovery regarding the absence of re-entrant granule profiles on some springtails. This discovery served to generalize the findings obtained in this work.

Prof. Hans Petter Leinaas at the Department of Biology, University of Oslo, has contributed with essential insights regarding the biological and evolutionary aspects of springtails. His helpful answers to my questions are greatly appreciated.

In the early stages of my thesis work, Kristian Greger Leinan took time to discuss and propose ways to simulate wetting on springtail cuticles computationally. Although this approach was not followed in the end, I am grateful for our interesting talks.

Last but not least, I would like to thank family, friends and classmates for their support and companionship.

Contents

1. Introduction

For over two thousand years, the self-cleaning ability of certain plant leaves has remained a mystery to mankind [1]. This lack of understanding can not merely be ascribed to a lack of human analytical capacity − by seeing the world through the lens of the human eye, man was simply not equipped for the task. Indeed, it was not until secondary electron microscopes (SEM) became commercially available in the late 1960s that the tool necessary for obtaining such an understanding was granted. Surpassing by far the resolution of the human eye, the introduction of the SEM revealed an essential feature of many plants and animals − namely, that they were covered by regular structure patterns, often hierarchical, at the micro- and even nanometer size scale [1]-[3] − some examples are given in Figure 1. What advantages lie behind an evolution of such intricate structural systems, and how can they translate into man-made technology? These questions have intrigued scientists and engineers in the recent decades, and the diversity in the answers reflects the diversity of nature itself.

In 1997, Barthlott and Neinhuis [2] discovered a peculiar effect on plant leaves with micro-sized wax crystals on their surfaces. In contrast to their smooth counterparts, they were, even after prolonged storage, almost completely free of contamination. An explanation to this self-cleaning ability was finally given, and at its heart lay the micro- and nanometer-sized sculpturing of the surface, rendering these plant leaves highly water repellent. Among the leaves demonstrating impressive self-cleaning were the leaves of the Lotus flower − an ancient symbol of purity in East Asian religions [3]; as a result, the term 'Lotus Effect' was coined. Almost concurrently, Onda et al. [8] showed − for the first time − that extremely water-repellent surfaces could also be manufactured *artificially*. During the last 15 years, these two reports have been followed by a steadily increasing research activity in a field that has become known as 'superhydrophobicity'[1] − the study and fabrication of extremely water repellent surfaces [1, 9, 10]. Fueling this interest is the vast potential of such surfaces in so-called 'biomimetic'[2] applications, of which the following accounts for only a non-exhaustive list: water repellent and self-cleaning textiles, windows, coatings and solar cells; micro/nanoelectromechanical systems with controllable wettability; microscale capillary engines for energy conversion and energy conservation; anti-icing, corrosion-resistant or current-reducing surfaces; and

[1] A quantitative criterion for labelling a surface 'superhydrophobic' will be given in Section 2.2.

[2] 'Biomimetics' refers to biologically inspired design, adaptation, or derivation from nature [6].

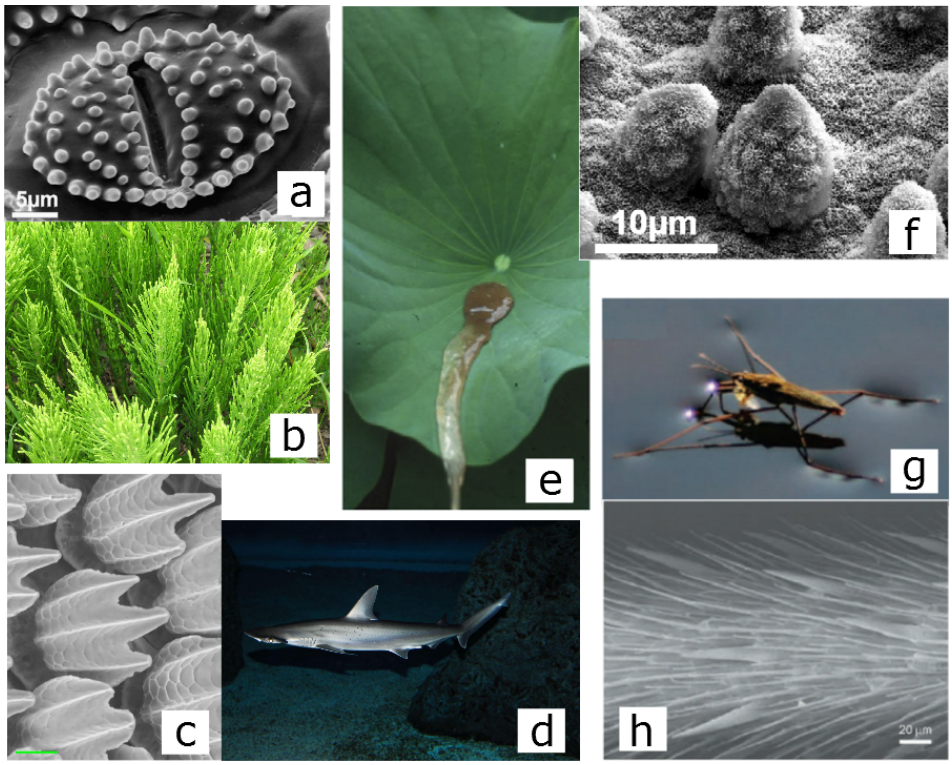

Figure 1: (a) Cuticle feature [4] of the plant *Equisetum arvenese* (b). (d) The skin of the bonnethead shark (*Sphyrna tiburo*) is covered by micro-sized denticles made of enamel and dentine (c) (scale bar: 50μm), reducing drag while swimming [5]. (e) Leaves of the lotus flower (*Nelumbo nucifera*) display self-cleaning behavior, due to a hierarchical structure at the micro- and nanoscale (f) [4]. (g) The legs of the water strider (*Gerris remigis*) [6] consist of numerous oriented microsetae (h) [6] (each of which are again covered by nanogrooves, not shown), estimated to yield a supporting force higher than 60 times the weight of its body [7]. Image (b) and (d) are licensed under the Creative Commons Attribution-Share Alike 2.0 Generic License [http://creativecommons.org/licenses/by-sa/2.0/deed.en].

ships, pipelines and microfluidic systems featuring significant reductions in hydrodynamic drag [1, 6, 9]-[13]. Indeed, various routes for achieving superhydrophobic surfaces have been identified experimentally in the recent years [1, 14]. Yet, large scale production of superhydrophobic surfaces that are also *mechanically durable*, remains a technological challenge [1, 14].

A natural surface that long has been known to be water repellent [15], is the cuticle (the 'skin') of arthropods called *springtails*, or *Collembolas* (Figure 2). Springtails are small (0.2 to 10 mm), wingless hexapods that are abundant on every continent on earth, including Antarctica [16]. Over 6 500 springtail species have been described, living in remarkably divergent habitats − although most numerous in soil, leaf litter and rotting wood, they are found even in glaciers, deserts and at altitudes above 7 700 meters in the Himalayas [16]. When springtails are studied in electron microscopes, striking micron- to sub-micron-sized patterns are revealed to exist on their cuticles [15]-[19] − Figure 2 presents an example of which. In combination with a wax layer covering all or part of the cuticle, these structural features are believed to be responsible for the springtail's non-wettable nature. Moreover, the detailed cuticle features vary among species. This is speculated to reflect adaptations for survival in dissimilar environments [15]-[19].

Recently, Helbig et al. [19] uncovered a notable characteristic of the granules on springtail cuticles; when cross-sectioned and viewed in a transmission electron microscope (TEM), they clearly displayed an *overhanging* or *re-entrant* profile (Figure 3). Furthermore, the authors argued that the existence of such overhangs could play a key role in making the springtails water repellent. Also importantly, a sand blast experiment was performed in order to assess the *mechanical* properties of the cuticles. The results suggested that springtail cuticles have a damage resistance that is clearly superior to that of the natural superhydrophobic surfaces found on plants. In light of the above-mentioned challenges in producing superhydrophobic surfaces that are also mechanically stable, this finding renders the springtail cuticle an eminent candidate for technological imitation.

Several prominent biological systems have been analyzed quantitatively in the last decade − let alone the superhydrophobic leaves of the Lotus flower [20]-[22], examples include the legs of the water strider, enabling it walk on water [7], the feet of the gecko, allowing it to climb vertical walls [23], and the spider web, demonstrating unique mechanical characteristics [24]. Drawing inspiration from these studies, we aim in the present study to do a thorough quantitative investigation of the wetting properties of

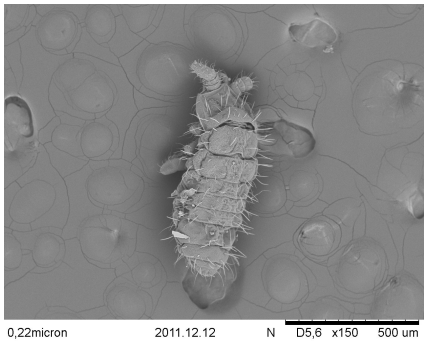

(a)

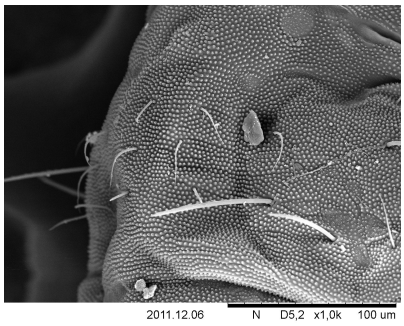

(b)

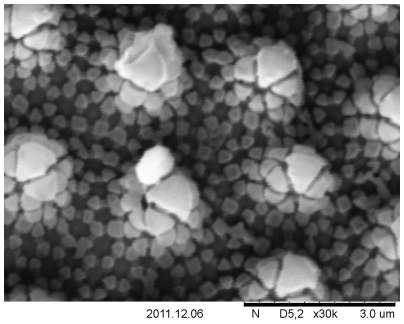

(c)

Figure 2: SEM images of the springtail *Hypogastura viatica*. (a) The full springtail body viewed from above. (b) Magnified view of the dorsal part (its 'back') of the springtail. Note the existence of micro-scale hairs (also visible in (a)) and so-called *secondary granules*, appearing as tiny, bright knobs in this image. (c) When zooming further in on the springtail cuticle, a networked pattern of smaller *primary granules* are revealed to exist between the secondary granules. While all springtail species feature primary granules, only some of them display secondary ones. See Appendix A for additional springtail images.

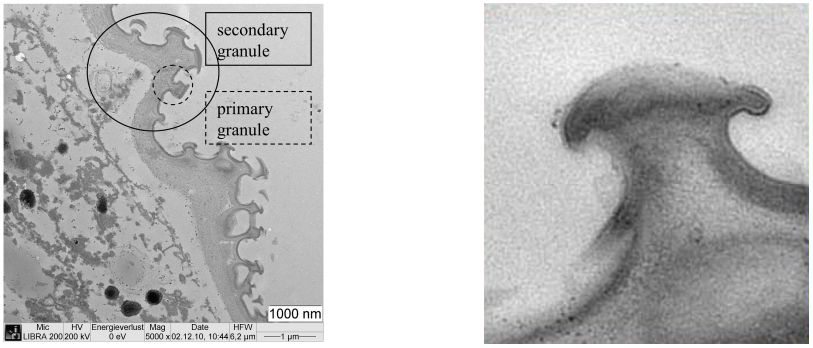

(a) (b)

Figure 3: (a) TEM image of a cuticle cross-section of the springtail species *Ceratophysella denticulata* [19]. (b) Magnified view of one of the primary granules present in (a), demonstrating an overhanging granule profile.

springtail cuticles. Such an analysis is desirable on many accounts. For instance, from a biological viewpoint, we may ask: what advantages − and disadvantages − lie in the variations seen among cuticle features of different springtail species, and how do these relate to their natural environments? Similarly, an engineer could restate the question as follows: which principles guide the non-wetting properties of springtail cuticles, and how may we employ these for technological purposes? And last, but not least − can springtail cuticles yield new clues about the physics of wetting phenomena on micro- and nanoscale-structured surfaces? These are questions that we wish to answer in this report.

The investigation will be based on a set of wetting measurements performed on nine different springtail species. SEM and AFM (atomic force microscopy) images will be used to evaluate each species' cuticle characteristics. Considering the finding by Helbig et al. [19] showing overhangs on cuticle granules, an assessment of the overhangs' alleged significance will be emphasized. Moreover, a recent study [25] has pointed out that *line energy* (in addition to *surface* energies) may be an important contributor to systems involving wetting phenomena on the micro- and nanoscale; the potential relevance of which for the case of springtails will comprise another area of focus.

The outline of the report is as follows. In Section 2, we review the most essential wetting theory for our cause. Next, we begin Section 3 by presenting the results obtained in the above-mentioned set of wetting measurements performed on nine springtail species. In the rest of Section 3, we use and develop theory with the purpose of explaining the

results of the wetting measurements. Finally, we draw conclusions and suggest directions for future research in Section 4.

2. Wetting on rough surfaces

In this section, we review wetting theory that are relevant for the discussion later in the report. Dusting off Young's statement from 1805 [26] is a natural starting point for that purpose.

2.1. Young's statement and its implications

When a small[3] droplet is placed or falls onto a smooth, solid surface, it takes the shape of a sphere that is sectioned by the surface [28]. At the three-phase contact line between the surface and the droplet (for short, the *triple line*), a measurable angle θ is then formed as portrayed in Figure 4 − this angle is termed *the contact angle*. In fact, this contact angle is used to determine whether a surface is *hydrophilic* (water loving) or *hydrophobic* (water fearing): hydrophilic surfaces form a contact angle with water *below* 90°, whereas hydrophobic surfaces attain contact angles *above* 90°. Young [26] stated that the contact angle is related to the liquid-air (F_{LA}), solid-liquid (F_{SL}) and solid-air (F_{SA}) surface tensions (force per distance solid-liquid-air contact line) by a force balance that mathematically is expressed[4]

$$F_{SA} = F_{LA}\cos\theta + F_{SL}. \tag{1}$$

Figure 4 serves as a sketch of the reasoning; Eq. (1) balances the forces acting on the triple line in the surface plane.

Contrary to Young's belief, however, a measurement of the contact angle θ for a given solid-liquid-air system will generally not be reproducible. Instead, if performing the same measurement repeatedly, one will obtain values in an interval $\Delta\theta$. In other words, there exists a *range* of stable contact angles for a given real surface. This phenomenon is also seen if the perimeter of a liquid droplet is forced to move, for example by tilting a surface holding a droplet (see Figure 5), or by adding or removing liquid to/from a droplet with a syringe or by condensation/evaporation. In such experiments, it turns

[3] A 'small' droplet is defined here as a droplet with a height smaller than twice the *capillary length* of the liquid. The capillary length of a liquid depends on the liquid's surface tension, its density and the gravitational acceleration. For water, the capillary length is about 2.7 mm [27].

[4] Often, Young's statement is paraphrased as concerning the three phases solid, liquid and *vapor*, or solid, liquid and *gas*. Young, however, considered the phases solid, liquid and *air* [26].

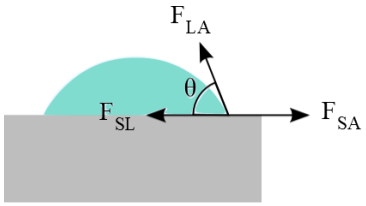

Figure 4: The forces acting on a solid-liquid-air contact line. F_{LA} = liquid-air surface tension, F_{SL} = solid-liquid surface tension and F_{SA} = solid-air surface tension.

out that for a given surface, the liquid tends to advance and recede at fairly constant contact angles − namely, with an advancing contact angle θ_a and a receding contact angle θ_r. It also turns out, that the contact angle observed for a static droplet can lie anywhere in between θ_r and θ_a [28]. The interval $\Delta\theta$ can thus be expressed as the difference $(\theta_a - \theta_r)$. The existence of this range of measurable contact angles is termed *contact angle hysteresis* (CAH) and will be discussed in greater detail in Section 2.3.

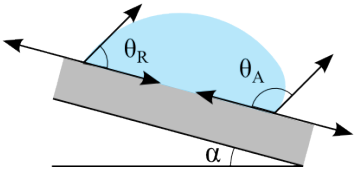

Figure 5: When the contact line of a droplet is forced to move, exemplified here by a tilted surface, the droplet generally recedes and advances under different contact angles. α measures the degree to which the surface is tilted. θ_r denotes the receding contact angle while θ_a denotes the advancing.

Now, if we assume that a given solid-liquid-air system is experiencing a specific contact angle θ, that may or may not be at equilibrium, we can also use the force balance in Eq. (1) to predict in which way the triple line will move, or if it will be stationary [29]. The range $\Delta\theta$ means that the surface tensions in Eq. (1) are to some extent adjustable. Their bounds are reached at $\theta = \theta_r$ in the one end, and at $\theta = \theta_a$ in the other end. Consequently, when the contact angle θ drops below θ_r, or extends beyond θ_a, the surface tensions are no longer able to adjust; they stay fixed. As a result, when a system displays a contact angle lying outside the interval $\{\theta_r, \theta_a\}$, a net force will be acting on the triple line. The direction of this force can be deduced from Eq. (1). By referring to Figure 4, we can summarize this as follows:

- When $\theta = \{\theta_r, \theta_a\}$, the triple line is stationary.

- When $\theta \geq \theta_a$, the triple line advances (moves to the right in Figure 4).
- When $\theta \leq \theta_r$, the triple line recedes (moves to the left in Figure 4).

These insights will be used extensively later in the report.

2.2. How roughness affects the contact angle

Real surfaces often exhibit roughness. Even though the contact angle *locally* still has to satisfy Young's statement (Eq. (1)), the roughness of a surface may modify the contact angle that is experimentally measurable − that is, the *macroscopic* or *apparent* contact angle, denoted θ^*. As indicated in the introduction, a rough surface is in fact crucial for achieving so-called 'superhydrophobic' surfaces − the definition of which relies on the ability of a surface to demonstrate $\theta^* > 150°$ when exposed to water [6, 10, 12]. However, the way in which the contact angle is modified depends on the way in which the droplet contacts the surface. Two classical equations for estimating the apparent contact angle − each corresponding to a specific droplet-surface contacting scenario − are the Wenzel equation and the Cassie-Baxter equation. These two equations are reviewed in the next two sections.

2.2.1. The Wenzel equation

One may, for example, visualize that the liquid penetrates between the solid rough asperities as such to make it completely in touch with the solid in the contact region (Figure 6). For this case, the Wenzel equation [30] predicts the apparent contact angle (with subscript W for 'Wenzel') as

$$\cos\theta_W^* = r\frac{\gamma_{SA} - \gamma_{SL}}{\gamma_{LA}} \tag{2}$$

where r is the *roughness coefficient*, defined as the ratio between the rough area of the surface and the area of the surface that would be projected into the surface plane, and where γ_{SA}, γ_{SL} and γ_{LA} are the solid-air, solid-liquid and liquid-air *surfaces free energies*, respectively. As has been noted by Gao and McCarthy [28], surface free energy (γ) and surface tension (F) are two different physical quantities, and should not be confused conceptually. Mathematically, however, they are equivalent [28], so for calculational purposes we may use $|\gamma| = |F|$. Then, Eq. (1) can be inserted into Eq. (2) to yield

$$\cos\theta_W^* = r\cos\theta, \tag{3}$$

where θ is the *local* contact angle, or equivalently, the contact angle that would be observed on a perfectly smooth surface ($r = 1$).

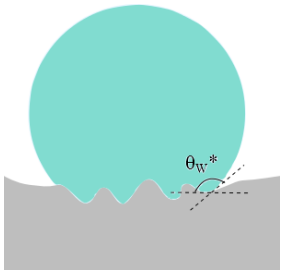

Figure 6: The Wenzel wetting state, characterized by physical contact between liquid and surface everywhere in the apparent contact area.

2.2.2. The Cassie-Baxter equation

Alternatively, one may imagine that the liquid droplet is sitting *on top* of the roughness asperities, with air pockets remaining beneath it (Figure 7). In such scenarios, the Cassie-Baxter equation can be used to predict the apparent contact angle. If f is the solid fraction of the surface (with surface areas measured as projected into the surface plane) and r_f is the roughness coefficient for this solid fraction, the apparent contact angle can be estimated as follows[5] (subscript CB for 'Cassie-Baxter') [31, 32]

$$\cos\theta_{CB}^* = -1 + f\,(r_f\cos\theta + 1) \tag{4}$$

There has been much discussion regarding the (range of) validity of the Wenzel and Cassie-Baxter equations [33]-[40]. Especially, it has been pointed out that only the surface properties *close to the droplet perimeter* are important in determining the apparent contact angle. Moreover, the droplet should be large compared to the roughness features

[5]Although this form of the Cassie-Baxter equation stems from Marmur [31], it is entirely equivalent to the original Cassie-Baxter equation [32] – also the original derivation by Cassie and Baxter considered a surface where the solid fraction was rough.

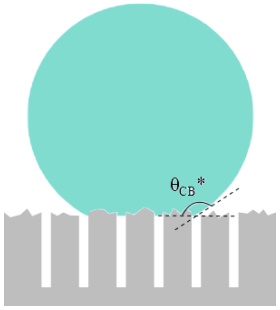

Figure 7: A Cassie-Baxter wetting state, characterized by the existence of air pockets between droplet and surface.

for the equations to apply. Still, the usefulness of these equations is unquestioned. As Gao and McCarthy states it, "they should be used with the knowledge of their faults" [33].

2.2.3. Incorporating line tension into the Cassie-Baxter equation

Three-phase line tension (for short, *line tension*) refers to the energy related to the line separating the three phases in a three-phase system. Figure 8 illustrates the concept and shows how line tension differs from surface free energy. Although line tension is well recognized and defined from a thermodynamic point of view (measured as energy per distance triple line), there is little consensus with regards to its magnitude; for solid-liquid-vapor systems (the other alternative being liquid-liquid-solid systems), values are reported in a range from 10^{-9} to 10^{-6} J/m [41]. Moreover, the effect of line tension is often neglected when analyzing wetting phenomena. However, for systems containing very small structures, the amount of triple line may become so large that the resulting line energy can not be ignored without causing serious errors in the evaluation of the system. Recently, Zheng et al. [25] argued that this would be the case when liquid droplets rest upon very small roughness asperities. Consequently, an estimation of the apparent contact angle for such systems should not only consider surface free energies, but also line tension. To achieve this, they introduced a modified Cassie-Baxter equation written (subscript Z for 'Zheng')

$$\cos\theta_Z^* = -1 + f\left(\cos\theta + 1\right)\left(1 - \frac{l}{S}\right), \tag{5}$$

where S is a *roughness scale* equal to the ratio between the area A_{solid} and the perime-

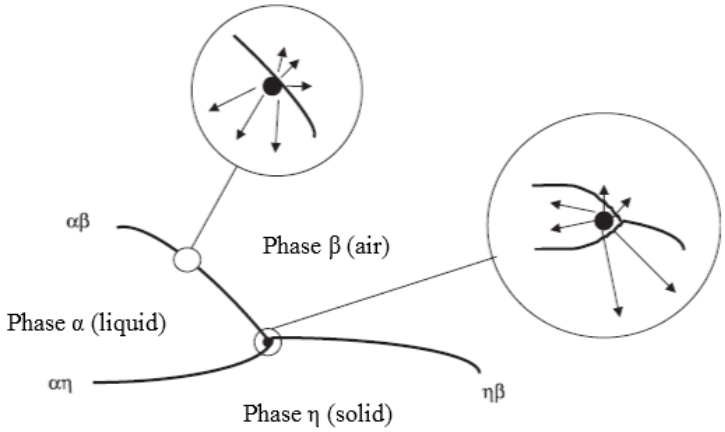

Figure 8: The understanding of three-phase line tension, and its relationship to surface free energy. *Left circle*: The well-known concept of surface free energy (γ) [J/m^2]. Molecules at a surface (or interface) neighbor less molecules identical to themselves than the molecules in the interior of the phase do − the surface molecules exist therefore at a higher energy level. *Right circle*: The often ignored concept of three-phase line tension (λ) [J/m]. Liquid phase molecules near the three-phase contact line are situated in a neighborhood that is fundamentally different from that of the 'ordinary' surface molecules sketched in the left circle − these 'three-phase molecules' neighbor molecules from all three phases and have a lower number of neighbors identical to themselves than the 'surface molecules' (left circle). They are thus at a distinct energy level, giving rise to the theory of three-phase line tension. Adapted from Amirfazli et al. [41].

ter L of the roughness asperities (see Figure 9), and where l is a 'chemical length' defined by

$$l = \frac{\lambda}{\gamma_{LA} + \gamma_{SA} - \gamma_{SL}} \tag{6}$$

where in which λ [J/m] is the magnitude of the three-phase line tension. The author of this report prefers to write Eq. (5) in an equivalent form[6]

$$\cos\theta_Z^* = -1 + f\left(r_f \cos\theta + 1 - \frac{\lambda}{S\gamma_{LA}}\right), \tag{7}$$

to avoid the intermediate calculation of l. From either form (Eq. (5) or Eq. (7)) it follows that a decreasing roughness scale S is accompanied by an increased apparent contact angle θ^*. This means that *small roughness asperities*, leading to low values[7] for $S = A_{solid}/L$, are predicted to increase the apparent contact angle.

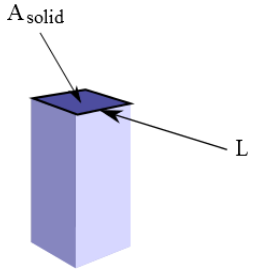

Figure 9: When a droplet exists in a Cassie-Baxter state, it sits upon roughness asperities; one of which is shown in the figure. The droplet contacts a roughness asperity area A_{solid}. The perimeter of the roughness asperities are denoted L.

To test this finding, Zheng et al. went on to fabricate a set of model surfaces featuring gradually decreasing roughness scales S. Owing to the lack of consensus regarding the line tension's magnitude, they used line tension as a *parameter* for explaining apparent contact angles that were measured experimentally on the fabricated surfaces. By doing so, a line tension magnitude of 1.57×10^{-8} J/m was found to yield a good general

[6] In line with Eq. (4), the factor r_f has been included in Eq. (7). This generalizes Eq. (5) to cases where the solid fraction of the surface is rough.

[7] This follows by considering that asperity area (A_{solid}) scales with asperity width to the second power, whereas asperity perimeter (L) scales with asperity width to the first power.

agreement between experiments and theory (Eq. (5)). However, the relation did not hold for surfaces with roughness scales S below 300 nm, for which Eq. (5) would predict apparent contact angles to reach 180°. Instead, a slight decrease in apparent contact angle was observed for these surfaces. Long-range hydrophobic interaction forces were proposed to explain this deviation.

Eqs. (3), (4) and (7) will come in handy in Section 3.2, where apparent contact angle measurements performed on nine springtail cuticles will be analysed.

2.3. Contact angle hysteresis (CAH)

As was mentioned in Section 2.1, real surfaces generally show a range $\Delta\theta$ of stable contact angles − a phenomenon termed *contact angle hysteresis*. The magnitude of CAH is related to the *roll-off angle* of a surface, defined as the angle to which a surface needs to be tilted (the angle α in Figure 2.3), in order for a water droplet to roll off. A low roll-off angle is essential in many natural and technological systems; for instance, efficient self-cleaning abilities require a roll-off angle below 10° [6]. Accordingly, a low CAH accounts for an important water repellent property. This motivates a review of CAH theory in this section.

2.3.1. Is CAH understood?

Before discussing the origins of CAH, however, a debate in today's research community should be mentioned − namely, the debate on whether or not contact angle hysteresis is in fact understood. One could ask: what counts as an 'understanding' of CAH? Quéré [42] states his view on this question in this way: "The contact angle hysteresis still remains in many cases an open problem − the problem being, for a well-characterized substrate composed of many defects, calculating the corresponding hysteresis". Gao and McCarthy seems to be of a different view as to what counts as an understanding of the subject. In their 2006 article titled "Contact Angle Hysteresis Explained" [43], arguments are put forth that CAH can be understood from perspectives of the three-phase contact line and of the kinetics of the contact line's motion. Still, no quantitative model for calculating the hysteresis is presented in the article, rendering the objective − as stated by Quéré − not yet accomplished. From the experimental perspective, Bormashenko et al. [44] have investigated to what extent different experimental techniques for measuring CAH produce the same results. They found that different experimen-

tal techniques supplied very different CAH values for the same surface, and concluded that "the CAH phenomenon is not profoundly understood from both experimental and theoretical points of view". Similarly, Marmur declared in a recent review [45] that "unfortunately, a comprehensive theory of CA hysteresis has not yet been developed, although some initial steps have been taken". This statement was later criticized by Gao and McCarthy [28], who held that "hysteresis is trivial to explain from the perspective of the contact line, and we do not believe that any theory will be very useful". In other words, the quality of the current understanding of CAH is disputed. Nevertheless, what is certain is that the efforts to increase our understanding of CAH did not end with Gao and McCarthy. The annual output of articles concerning CAH has increased steadily throughout the last decades, and has never been higher than in the last few years. The rich diversity seen in the approaches employed to study CAH − examples include phase-field models [46, 47], molecular dynamics simulations [48, 49], lattice Boltzmann methods [50, 51], as well as numerous mechanical [42, 52]-[57] and thermodynamic [58]-[64] analyses − illustrates the complexity of the problem. Especially interesting for our cause are two recent models [57, 62] for predicting CAH for the special case of surfaces where water generally exists in the Cassie-Baxter state. These two models will be reviewed in Section 2.4.

2.3.2. The origins of CAH

We now return to the question of what causes CAH. Proposed explanations can be categorized into two mechanisms [6, 65]: manifestation of the so-called adhesion hysteresis, and mechanical pinning of the contact line by localized defects. Adhesion hysteresis is an effect originating at the molecular level and is caused by a restructuring of the liquid-solid interface over time. As a result, work required to separate two surfaces (receding edge of a droplet) exceeds the energy gained when the surfaces come together (advancing edge of a droplet) [66]. This effect can explain why there usually exists some 'intrinsic' CAH even on chemically and physically defect-free (that is, smooth and homogeneous) surfaces; following wetting of a solid surface, the solid-liquid interfacial tension F_{LS} changes to, say, F'_{LS}. By Young's statement (Eq. (1)), this translates into a change in the contact angle θ. Considering that an advancing contact line will experience the tension F_{LS}, whereas a receding contact line will experience the tension F'_{LS}, an intrinsic contact angle hysteresis is expected [65, 67].

Mechanical pinning of the contact line can occur either due to chemical or physical defects. The way in which such defects lead to CAH has been qualitatively well explained by Gao and McCarthy [43]. Consider first a moving droplet that approaches a *chemical* defect at the advancing edge of the contact line. Since this chemical defect is composed of a different material than the rest of the surface, this surface region displays (for instance) a higher advancing contact angle θ_a than the rest of the surface. This means, that for the droplet to advance over the defect, it must change shape to attain a higher advancing contact angle near the defect. On the other hand, if the defect approached by the advancing contact line displays a *lower* advancing contact angle than the rest of the surface, no shape change is necessary; by Young's statement (Eq. (1)), the criteria for advancing is satisfied. Hence, defects approached by the advancing contact line of a moving droplet will induce shape changes in the droplet that tend to increase the overall advancing contact angle. The same reasoning, but applied to defects approached by the *receding* edge of the contact line, shows that at this edge, defects will tend to *decrease* the overall receding contact angle. The combined effect is then that the hysteresis $\Delta\theta = (\theta_a - \theta_r)$ increases. *Physical* defects induce CAH in much the same way. When a moving contact line approaches an inclined region of the surface (a physical defect), the intrinsic advancing (or receding) contact angle must be satisfied *locally* to allow further motion of the line. To accomplish this, local shape changes of the droplet are (sometimes) required. By the same arguments as those presented above, there will be a tendency for the advancing angle to increase and for the receding angle to decrease − hence contributing to contact angle hysteresis. For both chemical and physical defects, the corresponding kinetic energy barrier posed to a moving contact line can be deduced from the droplet shape change necessary to allow further motion: if ΔA is the amount of extra liquid-air surface involved in the shape change, the kinetic energy barrier can be expressed $\Delta E = \gamma_{LV}\Delta A$ [43].

2.4. CAH on composite surfaces

2.4.1. A differential Cassie model by Choi et al.

Having discussed the anticipated origins of CAH, we now consider the special case of CAH on composite surfaces. 'Composite surfaces' are understood here as surfaces where water droplets generally will exist in the Cassie-Baxter state. In this state, the apparent contact angle of the droplet have traditionally been calculated using the Cassie-Baxter

equation (Eq. (4)). However, the Cassie-Baxter equation does not predict the CAH that is usually evident also in this wetting state [62]. In light of this, Choi et al. [62] introduced in 2009 a modified Cassie-Baxter relationship, specifically tailored to explain the CAH on composite surfaces. Their idea was that f (and hence θ^*) in the Cassie-Baxter equation, the solid fraction of the surface, should not be calculated by considering the surface as a whole; rather, f should be calculated by considering the solid fraction of surface for a 'differentially small' displacement of the contact line. The important implication of this adjustment, is that f can attain different values at the receding and advancing edges of a moving droplet − and hence, different apparent contact angles at each edge. Denoting the two different solid fraction of surface parameters by f_a and f_r for the advancing and receding edge, respectively, they obtained the following expressions for the apparent contact angle at the advancing and receding edge:

$$\cos\theta_a^* = r_f f_a \cos\theta_1 + (1 - f_a)\cos\theta_2 \tag{8}$$

$$\cos\theta_r^* = r_f f_r \cos\theta_1 + (1 - f_r)\cos\theta_2 \tag{9}$$

It is in fact the Cassie equation for a heterogeneous surface [68], which is a generalization of the Cassie-Baxter equation reviewed in Section 2.2.2 (Eq. (4)), that has been modified by Choi et al. For surfaces consisting of solid structures separated by air, which is the situation that is relevant in our case, θ_2 is equal to 180° (contact angle for water in air). By setting $\theta_1 = \theta$ we can then write

$$\cos\theta_a^* = -1 + f_a\,(r_f \cos\theta + 1) \tag{10}$$

$$\cos\theta_r^* = -1 + f_r\,(r_f \cos\theta + 1) \tag{11}$$

which better elicits the similarity to Eq. (4). For the case of so-called 'discrete hoodoos' (square-shaped defects exhibiting an overhanging profile at the edges), Choi et al. evaluated f_a and f_r as illustrated in Figure 10. For a differentially small advanced distance ϵ, the triple line traverses a homogeneous air region (Figure 10a). Consequently, f_a is zero in this case (no solid fraction of surface). In contrast, for a differentially small *receded* distance ϵ, the triple line traverses a region with solid fraction equal to $f_r = 2W/(2W + 2D)$, where W is the half-width of the hoodoos and D is half the separation between two hoodoos (Figures 10b and 10c).

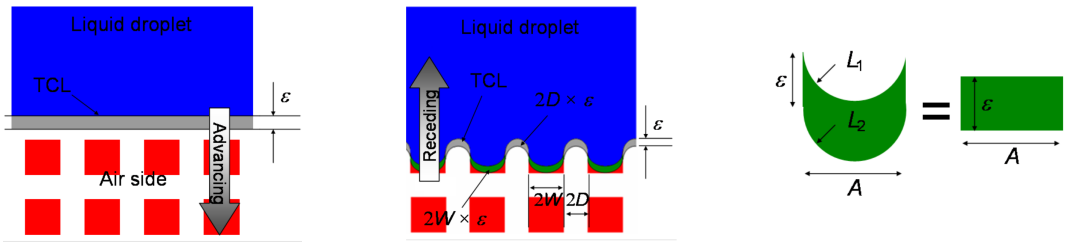

(a) (b) (c)

Figure 10: Calculation of the differential parameters f_a and f_r in Eqs. (10) and (11) [62]. (a) Calculation of f_a by considering a small triple line displacement at the advancing edge. (b) Calculation of f_r by considering a small triple line displacement at the receding edge. (c) Calculation of the area traversed in (b). TCL = Triple contact line, W = half-width of one hoodoo and D = half the separation between neighboring hoodoos.

CAH is then predicted on the basis of the different values for f_a and f_r, and hence also for θ_a^* and θ_r^*. To evaluate this model, microstructured composite surfaces of various geometries were fabricated. Contact angle measurements on these surfaces showed that the theory was in good agreement with experimental findings. For some of the surfaces, however, including the discrete hoodoos, the measured advancing contact angle was somewhat lower (164°) than predicted by the model (180°). This discrepancy was ascribed to vibrational perturbations from the laboratory environment, allowing the droplet to partially relax.

The approach to CAH presented in this section will from now on be referred to as *the Choi model*.

2.4.2. A mechanical approach by Dufour et al.

A different approach to describe CAH on composite surfaces has been taken on by Dufour et al. [57]. By building upon earlier work by Joanny and de Gennes [69] and Reyssat and Quéré [53], and by utilizing SEM images of UV-cured polymer droplets sitting on top of microstructures (Figure 11), they attempted to evaluate the magnitude of the 'deformed' liquid-air interface area (ΔA) at the receding edge of a tilted droplet (Figures 11b and 11c).

As noted earlier by Gao and McCarthy [43], the required 'deformation energy' for a

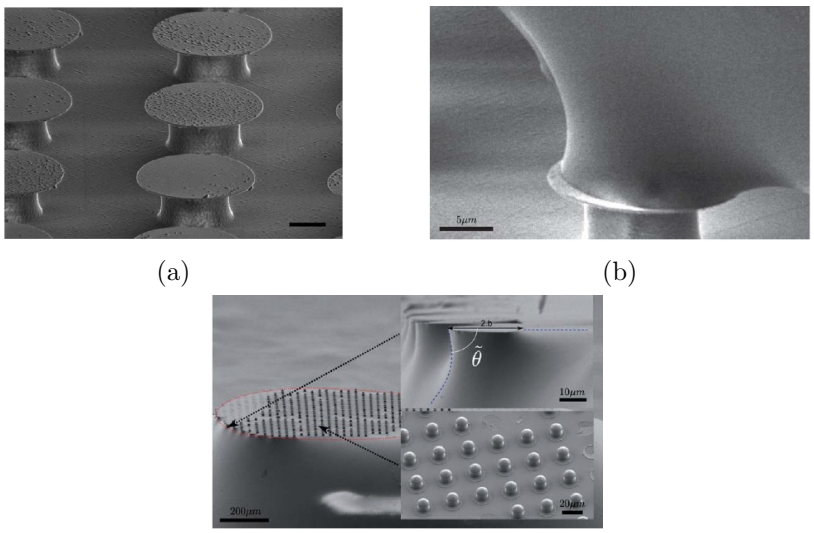

(a) (b)

(c)

Figure 11: (a) Microstructures fabricated by Dufour et al. [57]. The scale bar equals 5 μm. (b) SEM image of the receding edge of a tilted and cured polymer droplet sitting on top of the microstructures shown in (a). (c) Underside of a tilted and cured polymer droplet. Note that the microstructures have been ripped out of the underlying substrate and appear as knobs. $\tilde{\theta}$ denotes the local receding contact angle.

deformed liquid-air interface can then be calculated as $\Delta E = \gamma_{LV} \Delta A$. After employing also the Furmidge equation [70], which relates the force per unit contact line length required to move a droplet, to the droplet's CAH, they obtained the expression

$$\Delta \left(\cos \theta^* \right) = \frac{\Delta A}{p^2} \tag{12}$$

where $\Delta \cos \theta^* = (\cos \theta_r^* - \cos \theta_a^*)$ is an indirect measure of the CAH and where p is the pitch between the microstructures (see Figures 11a and 12a). The challenge in using this model is the calculation of the deformation surface area (ΔA). To do this, SEM images of tilted and UV-cured polymer droplets were captured and analyzed (Figure 11b). Based on these images, the deformation surface area caused by one single defect was estimated by an area described by a semi-revolution of the so-called catenary curve (Figures 12 and 13).

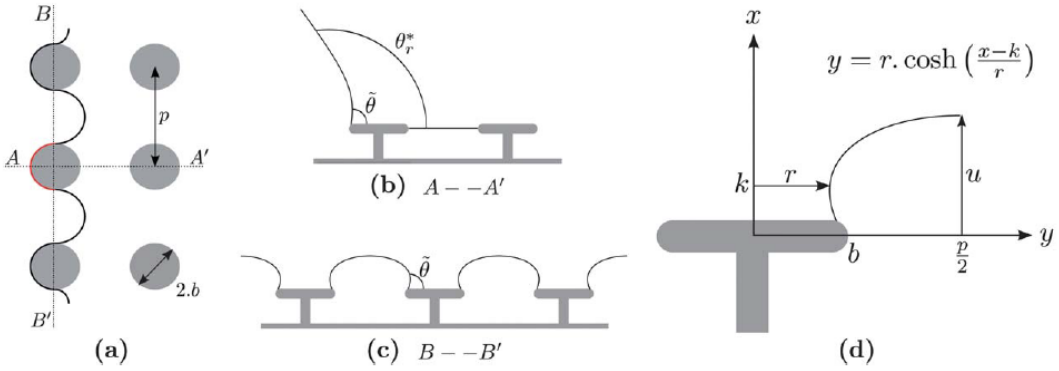

Figure 12: Schematics of the deformation surface area (ΔA) calculation [57]. (a) Top view of the microstructures (grey circular disks) and the droplet's contact line (solid line) at the receding droplet edge. (b) Side view of the liquid-air interface at the receding edge of the droplet. $\tilde{\theta}$ is the local receding contact angle, whereas θ_r^* is the apparent (macroscopic) receding contact angle. (c) Seeing the droplet 'from behind', focusing on the shape of the liquid-air interface (solid line) between the microstructures. Compare with Figure 11c. (d) Magnified view of (c), showing the shape of the modelled liquid-air interface at a single defect, and highlighting the parameters used in the calculation of ΔA.

The catenary curve can be described analytically as

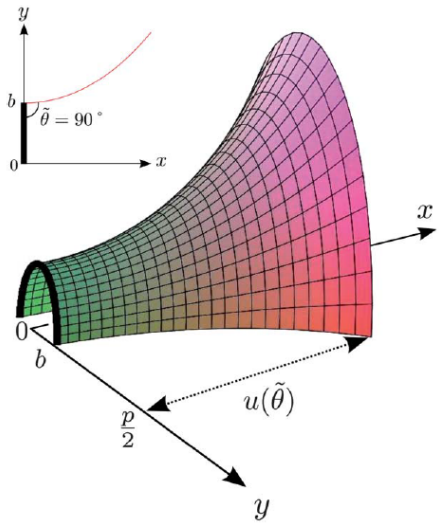

Figure 13: A numerical estimate of the area of a semi-revolved catenary curve for the special case of $\tilde{\theta} = 90°$. [57]

$$y = r \cosh\left(\frac{x-k}{r}\right), \tag{13}$$

where the parameter r is the 'waist radius' of the catenary curve and the parameter k is the catenary center (the point on the x-axis corresponding to the minimum y value, see Figure 12d). These two values can be computed by taking into account the boundary conditions $y(0) = b$ and $y'(0) = \tan\left(\frac{\pi}{2} - \tilde{\theta}\right)$, where b refers to the half-width of each defect and $\tilde{\theta}$ refers to the local (intrinsic) receding contact angle (Figure 12). Following this, the deformation surface area ΔA can be calculated as

$$\Delta A = \int_0^{\pi} \int_0^{u} \left(y(x)\sqrt{1 + y'(x)^2}\right) dx d\theta \tag{14}$$

where u is the maximal deformation between two defects (see Figures 12 and 13) and can be evaluated as [57]

$$u = k + r \ \text{arccosh}\left(\frac{p}{2r}\right). \tag{15}$$

A numerical solution of Eq. (14), for the case where $\tilde{\theta} = 90°$, is shown in Figure 13. After ΔA has been calculated, Eq. (12) can be used to obtain an (indirect) prediction

of the CAH. Dufour et al. used this approach to study how the local contact angle $\tilde{\theta}$ affects the CAH on such surfaces. This approach will be referred to in the following as *the Dufour model*.

2.5. Stability of a metastable Cassie-Baxter state

To motivate our interest in the stability of a metastable Cassie-Baxter state, it is necessary to reveal a finding that will be made later in the report − namely, that water droplets seem to exist in a *metastable Cassie-Baxter state* on springtail cuticles. This means that an energy barrier is preventing the system from transitioning to a Wenzel state that is − in this case − lower in energy than what the Cassie-Baxter state is. In fact, this feature is not unique for springtails − it is shared with several other synthetic and natural wetting systems [71]. Since a Cassie-Baxter state is considered to be required for achieving superhydrophobic properties [72, 73], the stability of such metastable Cassie-Baxter states has received much attention in the recent years [71].

How should the energy barrier against a transition from a Cassie-Baxter state to a Wenzel state be evaluated? The answer to this question depends on how the transition occurs. This, again, is related to what kind of stimulus it is that *drives* the transition. In a recent review on the topic, Bormashenko et al. [71] lists the following stimuli that have been observed to cause this so-called 'Cassie-Wenzel transition': droplet gravity, pressure applied to the liquid phase, droplet impact, droplet evaporation, electric fields in electrowetting experiments, and vibration of droplets. For understanding apparent contact angle measurements performed on springtail cuticles, droplet gravity is the relevant stimuli. However, for illuminating how the wetting properties of springtail cuticles affect the springtail's life in nature, or, analogously, for evaluating potential applications of springtail-inspired engineered surfaces, it would also be interesting to investigate the stability of the Cassie-Baxter state in outdoor and underwater scenarios. For this purpose, the effects of droplet impact (e.g., rain) and immersion will be considered as well.

2.5.1. Cassie-to-Wenzel transition mechanisms

Droplet gravity, immersion and droplet impact is treated here as sources to an increased hydrostatic pressure in the liquid phase, resulting in a pressure difference ΔP across the interface separating the liquid and the air pockets beneath it (assuming a Cassie-Baxter state). The problem can then be restated as follows: how high a hydrostatic

pressure is the liquid-air interface able to support? This leads us back to the question of how the transition occurs. Two transition mechanisms that are physically realistic[8] and often proposed [29, 79]-[86] in the case of a hydrostatic pressure, are *sag transitions* and *de-pinning transitions* [86]:

Sag transition If there exists a pressure difference ΔP across a liquid-air interfacial element, the Young-Laplace equation [87] predicts the equilibrium curvature of the element to be described by

$$\Delta P = \gamma_{LV} \left(\frac{1}{R_1} + \frac{1}{R_2} \right), \tag{16}$$

where γ_{LV} is the surface free energy of the liquid-air interface and where R_1 and R_2 are the principal radii of curvature of the element (Figure 14). When the Young-Laplace equation is applied to a liquid droplet sitting on a composite surface, it implies that if the hydrostatic pressure of the droplet is greater than the air pressure beneath it, the liquid-air interface will (in equilibrium) show a net deflection down towards the bottom of the substrate. Thus, the liquid-air interface will exhibit a *sag distance* (Figure 15a). When this sag distance becomes greater than the height of the roughness features, the liquid will touch the substrate bottom. As this happens, it has been observed [73, 88, 89] that the system undergoes a transition from a Cassie-Baxter to a Wenzel state (assuming, still, a *metastable* Cassie-Baxter state).

De-pinning transition A change in the curvature of the liquid-air interface will also induce a change in the local contact angle θ (Figure 15b). As discussed in Section 2.1, if θ increases such that $\theta \geq \theta_a$, it follows from Young's statement that the triple line will advance. Hence, the triple line will no longer be pinned at its original position. If the shape of the roughness features allows it, the triple line may advance the whole way down to the substrate bottom. In that case, a de-pinning transition has taken place.

In many cases, both sagging and de-pinning mechanisms will be involved in a Cassie-Wenzel transition. The relative importance of each mechanism is determined by the chemical properties of the system (through γ_{LV}, θ_r and θ_a) and by the shape of the roughness features that are bridged by the liquid-air interface. It should be noted that

[8] Indeed, many other proposed transition mechanisms [74]-[78] are in violation with Young's statement and/or the Young-Laplace equation (Eq. (16)).

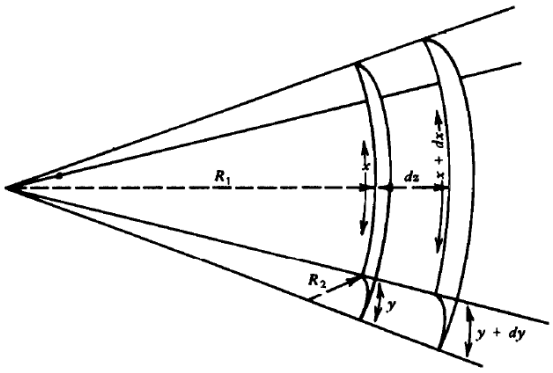

Figure 14: An interfacial element expanding due to a pressure difference across the interface [87]. R_1 and R_2 are the principal radii of curvature of the element. They are regarded as positive when the interface bends towards the air phase.

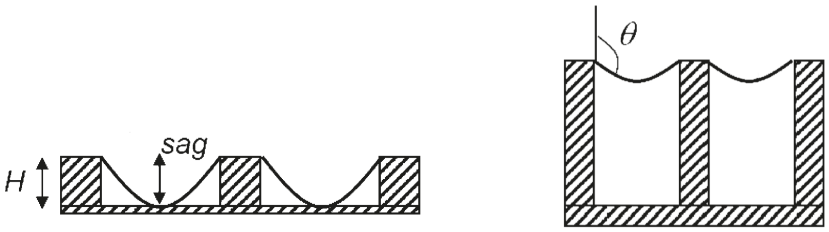

(a) Sag transition (b) De-pinning transition

Figure 15: Two general mechanisms that can lead to a Cassie-Wenzel transition, resulting from a hydrostatic pressure. Adapted from Patankar [86].

these mechanisms are relevant for all kinds of roughness features, not only for straight-walled features as those depicted in Figure 15.

2.5.2. How to estimate the Cassie-Baxter state stability

Having discussed probable mechanisms for a system to undergo a Cassie-Wenzel transition, we are now ready to analyze the stability of the Cassie-Baxter state quantitatively. Two useful approaches for this purpose will be reviewed in the next two sections. In these approaches, the Cassie-Baxter state stability is evaluated in terms of the *maximum pressure difference* that the system can sustain, without transitioning into a Wenzel state. Indeed, this way of measuring the stability is the most appropriate in our case; the maximum pressure difference estimates can easily be compared to the hydrostatic pressure that arises from droplet gravity, immersion, or droplet impact.

2.5.3. De-pinning and sagging predicted by the Young-Laplace equation

As described in Section 2.5.1, a pressure difference across a liquid-air interface gives rise to a curved liquid-air interface, and the pressure difference and the curvature of the interface are related by the Young-Laplace equation (Eq. (16)). In fact, by employing boundary conditions specific to the surface, the Young-Laplace equation makes it possible (at least in principle) to determine the spatial distribution of the liquid-air interface for a given surface geometry and a given pressure difference. Both the sag distance and the change in local contact angle, resulting from a pressure difference, are geometrically related to the spatial distribution of the liquid-air interface. Thus, if one is able to solve the Young-Laplace equation in the relevant spatial region, one can obtain the sag distance and the change in contact angle for a given pressure difference. Subsequently, the sag distance can be compared to the height H of the roughness features of the surface, and the changed contact angle can be compared to the advancing contact angle θ_a. The former comparison will serve as a prediction of a sag transition, while the latter will estimate the onset of a possible de-pinning transition. Luo et al. [29] have performed a theoretical analysis in this way for the case of micro-structured striped surfaces. By studying such a surface, they could approximate the liquid-air interface shape well by considering only *one* radius of curvature − hence simplifying the problem significantly. Experimental investigations on PDMS surfaces fabricated with a similar structure showed good agreement with the theoretical analysis [29].

An advantage by using this approach, is that both sag transitions and de-pinning transitions can be predicted. A disadvantage is the need for determining the spatial distribution of the liquid-air interface, which can be demanding for a three-dimensional system. However, as mentioned above, if considering only a two-dimensional system, there is only one radius of curvature that comes into play in the Young-Laplace equation (Eq. (16)). This simplifies the problem substantially. In Section 3.3.1, such an approach will be used to construct a two-dimensional model for determining the Cassie-Baxter state stability on springtail cuticles.

2.5.4. Direct relation between pressure difference and surface tension

A simpler approach to this problem was proposed by Zheng et al. in 2005 [79]. Their claim was that the downward force on the liquid-air interface, produced by the pressure difference ΔP, had to be balanced by the force represented by the vertical component of the liquid-air surface tension F_{LA} along the triple line (taking the surface plane as the *horizontal* direction), for the liquid to remain pinned on top of the roughness features. The situation is illustrated in Figure 16, which depicts a repetitive unit of a composite surface. The repetitive unit contains *one* roughness feature and its associated space around it. The roughness feature is partially wetted by a liquid phase that is pressed down from above. Now, let A be the area corresponding to a horizontal cross-section of the repetitive unit, let A_{solid} be the horizontal cross-section area of the roughness feature and let L be the total triple line length contained in the repetitive unit. The balance stated by Zheng et al. can then be expressed in mathematical terms by

$$\Delta P\,(A - A_{solid}) = -LF_{LA}\cos\theta, \tag{17}$$

giving

$$\Delta P = \frac{-LF_{LA}\cos\theta}{(A - A_{solid})} \tag{18}$$

for the maximum sustainable pressure difference (note that $\cos\theta < 0$ for a hydrophobic surface, as is considered here). By employing this simple 'force balance', they obtained the same maximum pressure difference as that calculated by a method similar to that described in Section 2.5.3. Since then, several other groups have used the same argument

[82, 83, 84]. It is interesting, however, that a proper motivation for this relation was not given before 2010 in a study by Afferrante et al. [84]. In fact, the 'force balance' presented by Zheng et al., and restated later by Wang et al. [83] and by Tuteja et al. [82], can not simply be understood as a force balance − the obvious reason for this, is that the force due to the hydrostatic pressure, acting on the liquid-air interface, and the force resulting from the vertical component of the liquid-air surface tension, *act in the same direction* − down towards the substrate. Nevertheless, the relation as stated in Eq. (18) is correct, as was shown by Afferrante et al. as follows:

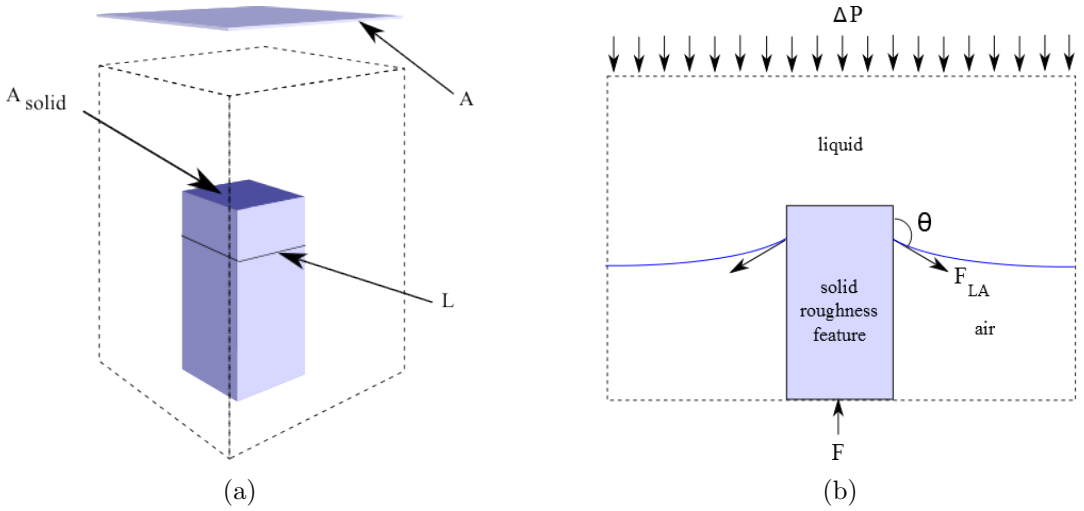

Figure 16: Schematics used in the derivation of a direct relation between the pressure difference (ΔP) and the liquid-air surface tension (F_{LA}). (a) 3D-view of a repetitive unit (dashed line) of a composite surface, containing one roughness element and its associated space. The solid line corresponds to the triple line. The liquid-air interface is not shown. (b) 2D-view of the same repetitive unit (dashed line), highlighting the forces at play (see text for more information).

First, the vertical forces acting on one of the roughness features of the surface are considered (Figure 16b). The hydrostatic pressure acts downwards on the roughness feature with a force $(\Delta P)\, A_{solid}$. Moreover, the downward vertical force on the roughness feature arising from the liquid-air surface tension is equal to $-LF_{LA}\cos\theta$ (Figure 16b) (note again that $\cos\theta < 0$ here). Finally, there must exist a force that makes it possible for the roughness feature to stay in place, even though it is being pushed down from above by the liquid phase. This is the upward force F, originating from the substrate beneath the roughness feature. In summary, we thus have the following force equation

for the vertical forces acting on one roughness feature:

$$(\Delta P)\, A_{solid} - L F_{LA} \cos\theta - F = 0 \tag{19}$$

Second, we zoom out and analyze the forces acting on the *entire repetitive unit* (Figure 16b). From above, we now have a force from the hydrostatic pressure that equals $(\Delta P)\, A$. From below, only the force F, originating from the substrate as before, is acting on the unit. For the entire repetitive unit to be in equilibrium, it is therefore required that $F = (\Delta P)\, A$. Taking this equality into account, Eq. (19) can now be written

$$(\Delta P)\, A_{solid} - L F_{LA} \cos\theta - (\Delta P)\, A = 0 \tag{20}$$

$$\Delta P\, (A - A_{solid}) = -L F_{LA} \cos\theta \tag{21}$$

$$\Delta P = \frac{-L F_{LA} \cos\theta}{(A - A_{solid})} \tag{22}$$

which is identical to the relation posed in Eq. (18).

The calculational simplicity of this approach comes at a price: by avoiding the evaluation of the spatial distribution of the liquid-air interface, one has no information available regarding the sag distance (Figure 15a). As a result, this approach can only be used to estimate the stability against a *de-pinning transition*.

In Section 3.3.4, this approach will be used to obtain a three-dimensional estimate of the Cassie-Baxter state stability against a de-pinning transition.

3. Wetting properties of springtail cuticles

3.1. Contact angle measurements on nine springtail species

In a study performed by our group, contact angle measurements[9] involving water droplets on nine different springtail species (Figures 20-28, Appendix A) supplied the results given in Table 1. Two general findings are immediately noticeable from the table: 1) Apparent contact angles are very high on springtail cuticles, and 2) With the exception of *Xenilla maritima*, springtail cuticles display very low contact angle hysteresis. In the following sections, our aim will be to use and develop theory that can account for these findings.

Table 1: Contact angle measurements on nine springtail species. (SG) signifies that the springtail species features secondary granules.

Springtail species	θ_r^*	θ_a^*	$\Delta\theta^*$
H. viatica (SG)	163.2	167.9	4.7
I. prasis	164.1	168.2	4.1
F. quadrioculata	166.5	171.0	4.5
A. septentrionalis (SG)	164.8	168.3	3.5
A. besellsi (SG)	164.5	169.6	5.0
C. clavatus	166.2	166.0	-0.2
A. laricis	161.2	157.4	-3.9
I. anglicana	158.6	154.3	-4.3
X. maritima	132.4	158.7	26.3

3.2. Explaining the high apparent contact angles

Table 1 shows that apparent contact angles are very high on springtail cuticles; indeed, many of them meet the criterion of being labelled *superhydrophobic* ($\theta^* > 150°$). As was also mentioned in the introduction, this non-wettable nature of springtail cuticles has been known for a long time. However, what causes these high apparent contact angles? This is what we seek to understand in this section.

[9]The advancing and receding contact angles were measured by use of a goniometer under addition and subtraction of water, respectively.

3.2.1. The chemical nature of springtail cuticles

As a starting point, we need to consider the chemical nature of springtail cuticles. Indeed, this has been paid some attention in the literature. Studies performed on the springtail species *Podura aquatica* and *Tomocerus flavescens* indicate, in similarity with what is found for many insects, that springtails feature a *wax layer* on their cuticles [15, 17]. Moreover, upon removal of this layer, it has been shown that the springtail's hydrophobic properties disappear [17]. It seems likely, therefore, that such a wax layer is present on the springtails considered in Table 1, allowing them to exhibit hydrophobic properties. By assuming the existence of a wax layer, a reasonable estimate for the intrinsic contact angles (i.e., the contact angles that would be observed on a smooth surface) on springtail cuticles can be obtained by considering contact angle measurements performed on smooth, waxy *insect* cuticles. Holdgate [90] found that such cuticles featured receding and advancing contact angles generally in the range of $90° - 100°$ and $100° - 110°$, respectively (the measurements were performed using water droplets, which is the relevant liquid also in our case). In line with this, we estimate that the springtail cuticles exhibit intrinsic receding contact angles of 95° and intrinsic advancing contact angles of 105°. Given these estimates, the chemical nature *alone* does not explain the high apparent contact angles observed on the springtail cuticles. As we saw in Section 2.2, however, the *roughness* of a surface does also affect the apparent contact angle. The effect of roughness on the apparent contact angle is therefore considered in the next section.

3.2.2. Effect of roughness on the apparent contact angles

In Section 2.2 we reviewed two classical equations for explaining how the roughness of a surface can affect the apparent contact angle − namely, the Wenzel equation (Eq. (3)), derived by assuming no air pockets between droplet and surface, and the Cassie-Baxter equation (Eq. (4)), where the opposite assumption is made (air pockets exist). We now wish to investigate whether these equations can shed light over the apparent contact angle measurements listed in Table 1.

To do so, however, a determination of the roughness coefficient (r) and the solid fraction of surface (f) is required for each of the springtail species[10] − this has been

[10]The roughness coefficient of the solid fraction (r_f) has been approximated as 1.

achieved by inspecting SEM and AFM images of the relevant springtails[11] (Figures 20-28 in Appendix A). For the springtails featuring secondary granules (denoted (SG) in Table 2), it has been assumed that water droplets are situated on top of these when calculating f. It should be noted that the contribution from hairs to these structure parameters has not been considered, and that it has been assumed that water droplets penetrate between the hairs (not sitting on top of them) when evaluating f. In fact, the studied springtails show a great diversity in their amount of hair (compare e.g. *Isotomurus prasis* (Figure 21a) and *Anurophorus septentrionalis* (Figure 23a)), while at the same time rather similar wetting characteristics (Table 1). Therefore, although the cuticle hairs are likely to affect the problem, they are not emphasized here[12]. Another comment that should be made, regards the fact that the Wenzel and the Cassie-Baxter equations do not consider contact angle hysteresis. Thus, only a single 'equilibrium' intrinsic contact angle θ goes into these equations. As a value for this angle, we use 100°, which is the average of the estimated receding and advancing intrinsic contact angles. Based on these assumptions, the Wenzel and Cassie-Baxter equations[13] predict apparent contact angles as given in Table 2. The *measured* apparent contact angles are repeated for comparison.

From Table 2, we first note that the Wenzel equation is not at all able to account for the contact angle measurements performed on the springtail cuticles. Hence, water droplets on springtail cuticles appear not to exist in a Wenzel state of wetting under normal laboratory conditions. On the contrary, water droplets should then exist in a Cassie-Baxter state of wetting, exhibiting air pockets between surface and droplet. However, the Cassie-Baxter equation does not predict correct apparent contact angles for all springtails − with the exceptions of *Archisotoma besellsi* and *Xenilla maritima*, the apparent contact angles are notably underpredicted. Different views may be put

[11] AFM images were not available for all considered springtails. As a result, height measurements were not possible to perform for all species. In these cases, average values of those obtained from other springtails were used.

[12] See Blow et al. [91] for a theoretical analysis of hairy surfaces.

[13] Regarding the validity in using these equations for springtail cuticles (see discussion in Section 2.2): We assume here that the surface parameters r, f and r_f are the same in the vicinity of the droplet perimeter as they are on the dorsal part of the springtail cuticles (their backs), as are imaged by use of SEM and AFM as shown in Figures 20-28 (Appendix A). Furthermore, it is noted that the roughness features of the cuticles are much smaller ($\lesssim \mu m$) than the water droplets used in the measurements ($\sim mm$), as required.

Table 2: Apparent contact angle predictions for nine springtail cuticles, based on the Wenzel equation (θ^*_W) and the Cassie-Baxter equation (θ^*_{CB}).

Springtail species	r	f	θ^*_W	θ^*_{CB}	θ^*_r	θ^*_a
H. viatica (SG)	2.19	0.16	112.4	150.2	163.2	167.9
I. prasis	1.16	0.17	101.6	149.3	164.1	168.2
F. quadrioculata	1.19	0.35	101.9	135.3	166.5	171.0
A. septentrionalis (SG)	1.71	0.31	107.3	138.1	164.8	168.3
A. besellsi (SG)	2.16	0.06	112.0	161.9	164.5	169.6
C. clavatus	1.35	0.44	103.6	129.5	166.2	166.0
A. laricis	1.18	0.64	101.8	118.1	161.2	157.4
I. anglicana	1.36	0.34	103.7	136.0	158.6	154.3
X. maritima	1.20	0.22	102.0	144.9	132.4	158.7

forward to explain these discrepancies. First of all, the approximate nature of the surface parameters r and f should be emphasized. As mentioned in Section 2.2, it is the surface characteristics *close to the droplet perimeter* that determines the wetting state of a droplet. One can not take for granted that the cuticle region considered when evaluating r and f in this study accurately represents the cuticle region where the droplet perimeter is settled in a contact angle measurement. In light of this, it is interesting to note that an experimental study performed in our group, recently showed that there indeed exists some variance in a springtail's cuticle features on the same animal [93]. Another complicating factor for determining surface parameters is the effect of hairs. That being said; it is difficult to comprehend how e.g. *Anurophorus laricis* (Figure 26 in Appendix A) − containing only a few hairs, and displaying quite densely packed granules − can support water droplets with a solid fraction of surface (f) below 0.08 − this would be required for the Cassie-Baxter equation to predict an apparent contact angle equal to that measured. There seems to be more to it.

3.2.3. Effect of line tension on the apparent contact angles

A second explanation concerns the concept of *line tension*, which was introduced in Section 2.2.3. The original Cassie-Baxter equation (Eq. (4)) does not take line tension into account. Yet, given the small (micron to sub-micron) size scale of the roughness features apparent on springtail cuticles, there will be a large total triple line length when a droplet exists in a Cassie-Baxter state on these features − thus permitting a prominent

role for line tension in determining the forces felt by the droplet perimeter. As described in Section 2.2.3, line tension can be incorporated in the Cassie-Baxter equation as given by Eq. (7). By using this equation, we now inquire what line tension magnitude is necessary for predicting apparent contact angles as those that are measured (Table 1). The results[14] are displayed in Table 3, which also includes the estimated roughness scale S for each species (determined, as before, by inspecting the SEM and AFM images in Figures 20-28 in Appendix A).

Table 3: Line tension magnitudes required for Eq. (7) to explain apparent contact angle measurements performed on nine springtail cuticles.

Springtail species	S [nm]	λ [J/m]
H. viatica (SG)	958	4.40×10^{-8}
I. prasis	576	2.67×10^{-8}
F. quadrioculata	463	2.61×10^{-8}
A. septentrionalis (SG)	1074	5.79×10^{-8}
A. besellsi (SG)	897	2.64×10^{-8}
C. clavatus	315	1.75×10^{-8}
A. laricis	625	3.31×10^{-8}
I. anglicana	350	1.49×10^{-8}
X. maritima	520	1.11×10^{-9}

Table 3 shows that a line tension magnitude of the order of 10^{-8} J/m makes it possible to explain the apparent contact angle measurements performed on springtail cuticles. This line tension magnitude is within the range of values that are reported in the literature [41], and correspond well with the magnitude recently found by Zheng et al. [25]. It is also noted that the roughness scales S are all greater than 300 nm, and are thus within the roughness scale range in which Zheng et al. found Eq. (7) to yield a good agreement between experiments and theory.

There is some variation in the values obtained for λ, however. This may again be a reflection of the difficulties in retrieving accurate surface parameters based on SEM and AFM images portraying only a very small region of the cuticle. Another possibility

[14]It is the averages of the measured receding and advancing apparent contact angles ($\frac{\theta_r^* + \theta_a^*}{2}$) that have been used to calculate the required line tension magnitude.

is that this variation arises due to differences between the springtails regarding their physical and/or chemical characteristics. After all, the nature of line tension is not fully understood, and its magnitude may well have dependencies that have not yet been revealed [41].

One important assumption made in this section has not been thoroughly discussed. This is the assumption that water droplets is situated in a Cassie-Baxter state (that is, the 'air pocket' state) on springtail cuticles, and not in a Wenzel state. Why should this be so? In fact, Patankar [92] has shown that the wetting state that predicts the lowest apparent contact angle, corresponds to the wetting state of lowest global energy. Thus, for springtail cuticles, a Wenzel wetting state yields the lowest global energy of the system − this state is the thermodynamically stable one. As was mentioned in Section 2.5, this renders the Cassie-Baxter state only *metastable*. This implies the existence of an energy barrier inhibiting the system from transitioning from the higher energy Cassie-Baxter state to the lower energy Wenzel state. This energy barrier is the subject of the following section.

3.3. How springtails hold water in a Cassie-Baxter state

In the case of a continuous liquid phase approaching the cuticle from above (which is the scenario relevant for us), it is clear that the system *initially* will exist in a Cassie-Baxter state, before a potential progression to a Wenzel state. But what constitutes the energy barrier working against such a transition? As discussed in the introduction, Helbig et al. [19] proposed − qualitatively − that the *overhanging profile* of the granules (Figure 3) can give rise to such an energy barrier. This proposition will be investigated in quantitative terms in this section.

Close to the completion of this report, however, an experimental study performed in our group [93] showed that *not all springtails exhibit overhangs on their granules*. Thus, for explaining the existence of an energy barrier, one can not rely solely on an overhanging granule profile for all of the springtails. It will be shown, however, that the exact same models as those that will be used and developed for an overhanging profile, also can be used to analyze the energy barrier caused by granules *not* exhibiting an overhang. Following this, it will be seen that re-entrant granules are in fact *not necessary* to explain the existence of an energy barrier. Re-entrant structures do affect

the Cassie-Baxter state stability, however. Thus, a quantitative consideration of this matter is still of relevance.

Interestingly, an article by Tuteja et al. [82] studies the stability of the Cassie-Baxter state on a surface containing roughness elements that are quite reminiscent of the springtail granules, and that study could potentially have served us here. However, this article suffers from some shortcomings. First, their starting point is a so-called "generalized force balance", stated without further motivation. This 'balance' corresponds to the direct relation between pressure difference and surface tension that was discussed in Section 2.5.4 (Eq. (22)). As we saw, this relation is in itself not a force balance. Still, the relation is correct, and can be used to predict the stability against a *de-pinning transition*. However, the way Tuteja et al. have employed the direct relation between pressure difference and surface tension is only valid in the limit where roughness element separations (denoted d_0 below) are infinitely larger than the radius describing the shape of the overhang (denoted r below). Second, by using the direct relation between pressure difference and surface tension, no information is available concerning the detailed shape of the liquid-air interface penetrating between the granules for a given hydrostatic pressure. Thus, the pressure necessary for inducing a *sag transition* can not be revealed easily. In an attempt to overcome this, a derivation involving several mathematical approximations are conducted, with the result being an approximate design parameter to guide in the stability against a sag transition *caused by gravity*. Hence, the study by Tuteja et al. can not be used to predict the Cassie-Baxter state stability of springtail cuticles under e.g. immersion or impact by rain droplets. A more general model is therefore required. In the following, such a model is presented, which not only predicts the stability against a de-pinning transition, but also the stability against a sag transition, for any source of hydrostatic pressure and without making mathematical approximations. The model is based on the approach outlined in Section 2.5.3.

3.3.1. 2D model of the springtail cuticle overhang

From Figure 3, it is seen that an important part of the overhang has a shape that can well be described by a circular arc. We use this observation to perform a two-dimensional consideration of the overhang's interplay with a liquid phase that approaches and eventually contacts the surface. Figure 17 sketches the situation. The liquid-air interface is regarded as flat (zero curvature) as it approaches the granules. Considering that the

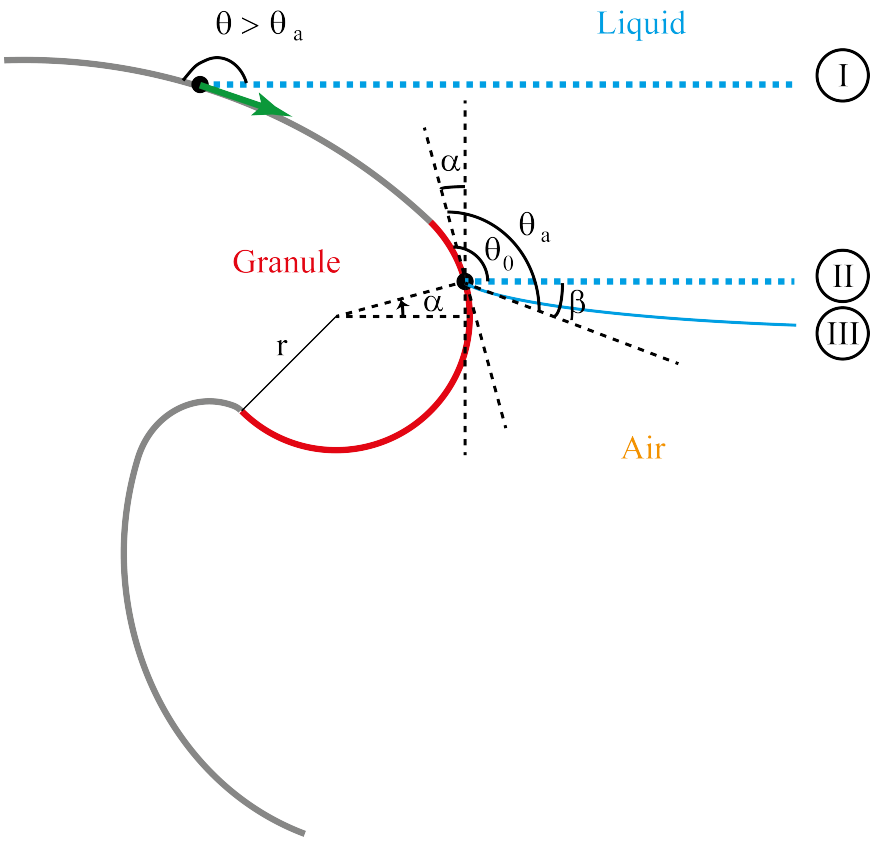

Figure 17: Evolution of the position and curvature of the liquid-air interface (blue lines) as it penetrates the granule pattern from above. The red part of the overhang is approximated as a circular arc, described by the radius r. See text for more information.

granules are in the micron to sub-micron size scale, this simplification is reasonable for a macroscopic liquid phase. Now, as soon as this flat liquid-air interface touches the granule, it will (in addition to F_{LA}) be subject to the surface tensions F_{SL} and F_{SA} at the triple line. Following this, the evolution of the triple line's position will thus be described by Young's statement (Eq. (1)) and its implications. At first, the contact angle (θ) is nearly 180° (event (I) in Figure 17). Since the advancing contact angle (θ_a) for springtail cuticles is estimated to be around 105°, θ exceeds θ_a. Young's statement then implies that the triple line advances until $\theta < \theta_a$. As the triple line advances, such a lowering of the local contact angle is naturally facilitated by the shape of the granule, ensuring $\theta < \theta_a$ at some point along the overhang. If no pressure difference across the liquid-air interface exists at this point, the local contact angle may settle anywhere in the interval $\{\theta_r, \theta_a\}$ – say, at θ_0 (event (II) in Figure 17). It is now assumed that the triple line is situated somewhere on the circular part of the overhang (this depends on θ_0, and is reasonable for $\theta_0 \lesssim 105°$). If imagining a circle segment as illustrated in Figure 17, we can now describe the triple line's position by the angle α, measured counter-clockwise from 'three o'clock' (by analogy to the unit circle).

For the triple line to advance further down the overhang, the criterion $\theta \geq \theta_a$ needs to be satisfied again. As was noted above, the Young-Laplace equation (Eq. (16)) predicts that if a *pressure difference* exists across a liquid-air interface, the interface will have a net curvature (in equilibrium). Specifically, if the hydrostatic pressure of the liquid phase is increased, leading to a pressure difference ΔP, the liquid-air interface will be forced to bend downwards. This increases the local contact angle θ by an amount β (event (III) in Figure 17). If the pressure difference becomes sufficiently high, θ will thus at some point reach θ_a again, allowing further advancement of the triple line. Once more, however, an advancement of the triple line will be associated with a decrease in the contact angle, due to the re-entrant geometry of the granule. Consequently, an even higher pressure difference is needed for the triple line to advance even further. The continued action of this mechanism makes the triple line effectively pinned on the granule until the pressure difference is so high that the triple line have advanced all along the overhang (by that time, however, a sag transition might have occured).

To obtain a quantitative measure of the pressure difference necessary for the triple line to advance to a given position α along the overhang, we use the Young-Laplace equation (Eq. (16)). Figure 18 aids in the derivation, displaying two granules with a liquid-air interface penetrating between them. As a result of a pressure difference ΔP,

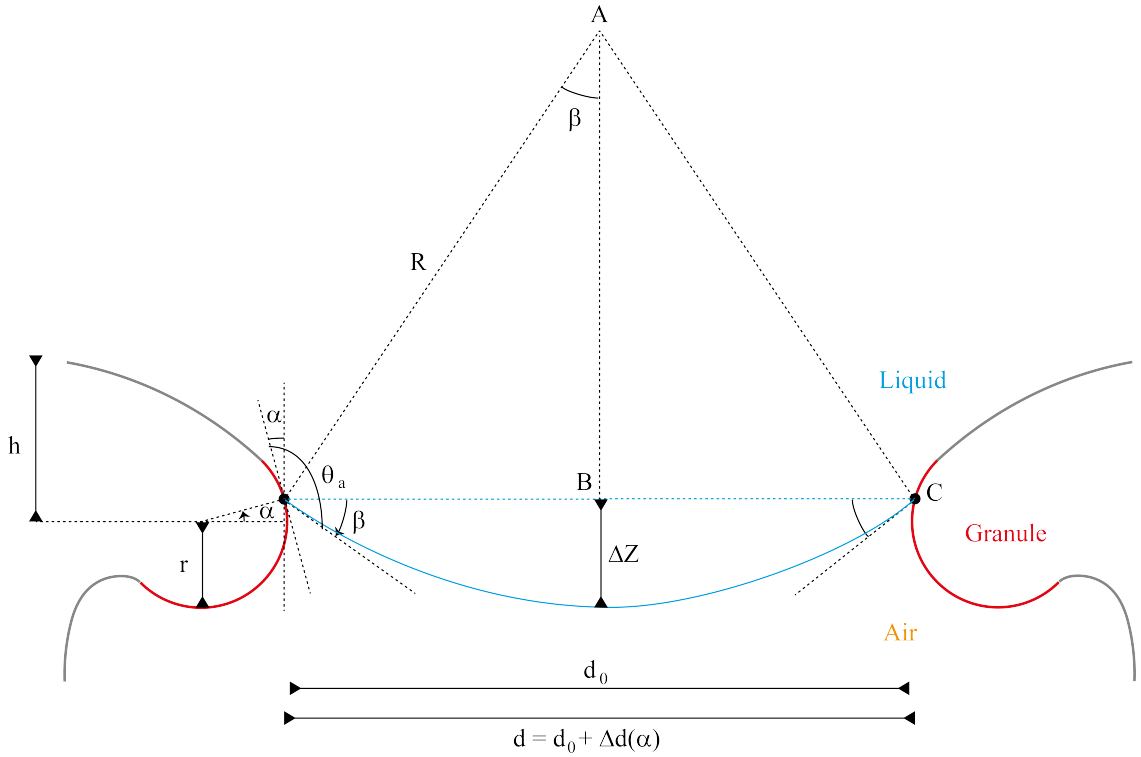

Figure 18: Geometrical relationships between the liquid-air interface curvature R, the sag distance ΔZ, the advancing contact angle θ_a and the triple line's position along the overhang, measured by the angle α. See text for a more detailed description.

the liquid-air interface is curved. In this two-dimensional consideration, the curvature of the liquid-air interface is described by only one radius of curvature, which is denoted here by R (perpendicular to the paper plane, the curvature is considered to be zero). The Young-Laplace equation then reads

$$\Delta P = \frac{\gamma_{LA}}{R}. \tag{23}$$

Now, to relate the pressure difference to the (equilibrium) triple line position, it is noted from Figure 18 that

$$\theta_a = \alpha + 90^\circ + \beta. \tag{24}$$

Moreover, it is seen that

$$\sin\beta = \frac{d/2}{R} \tag{25}$$

where d is the distance between the two granules, measured from the triple line position at each granule. By considering how this distance varies as the triple line changes position α along the overhang, we obtain

$$d = d_0 + \Delta d(\alpha) = d_0 + 2r\left[1 - \cos(\alpha - \alpha_0)\right] \tag{26}$$

where d_0 is the distance between the granules at $\alpha = 0$ (the shortest inter-granule distance), r is the radius of the circle describing the circular part of the overhang and α_0 is the initial triple line position on the overhang (the triple line position corresponding to $\theta = \theta_0$). From Figure 17 it is noted that $\alpha_0 = \left(\theta_0 - \frac{\pi}{2}\right)$. Thus, Eq. (26) can alternatively be written

$$d = d_0 + 2r\left[1 - \cos(\alpha - \theta_0 + \frac{\pi}{2})\right] = d_0 + 2r\left[1 + \sin(\alpha - \theta_0)\right]. \tag{27}$$

Furthermore, by taking the two-dimensional Young-Laplace equation into account (Eq. (23)), we can restate β as follows:

$$\beta = \arcsin\frac{d/2}{R} = \arcsin\frac{d\Delta P}{2\gamma_{LA}} = \arcsin\frac{\left[d_0 + 2r\left(1+\sin(\alpha-\theta_0)\right)\right]\Delta P}{2\gamma_{LA}}. \tag{28}$$

Inserting Eq. (28) into Eq. (24) results in

$$\theta_a = \alpha + 90^\circ + \arcsin\frac{\left[d_0 + 2r\left(1+\sin(\alpha-\theta_0)\right)\right]\Delta P}{2\gamma_{LA}}. \tag{29}$$

This equation can in turn be rearranged to give

$$\Delta P = \frac{2\gamma_{LA}\sin\left(\theta_a - 90^\circ - \alpha\right)}{d_0 + 2r\left[1+\sin(\alpha-\theta_0)\right]} = \frac{-2\gamma_{LA}\cos\left(\theta_a - \alpha\right)}{d_0 + 2r\left[1+\sin(\alpha-\theta_0)\right]}, \tag{30}$$

which relates the pressure difference ΔP to the triple line position α, as desired. The maximum pressure difference predicted by Eq. (30) corresponds to the pressure difference necessary for the triple line to slide past the entire overhang (assuming that this pressure difference is sustained). Thus, Eq. (30) can be used to estimate the stability of the Cassie-Baxter state against a *de-pinning transition*, provided values for d_0, r, θ_0, θ_a and γ_{LA} are available. Eq. (30) also reveals clues regarding what kind of surfaces will effectively resist de-pinning wetting transitions. For one, it is seen that *small granule separations* d_0 enhances the stability. Second, it is observed that the existence of an *overhang* enables the factor $[-\cos\left(\theta_a - \alpha\right)]$ to be maximized, due to the wide range of possible α implied by the existence of an overhang. The proposal by Helbig et al. [19] is therefore supported by this model, in that re-entrant granule profiles contribute to a more stable Cassie-Baxter state.

Furthermore, by using this model we can also calculate the sag distance (ΔZ in Figure 18) and predict the stability against a *sag transition*. For this purpose, we start by employing the Pythagorean theorem to the triangle ABC in Figure 18 and realize that the distance AB is equal to $(R - \Delta Z)$ when $0^\circ < \beta < 90^\circ$ and $(\Delta Z - R)$ when $\beta > 90^\circ$. This allows us to express ΔZ in terms of d and R as

$$\Delta Z = R - \sqrt{R^2 - \left(\frac{d}{2}\right)^2} \qquad \text{when} \qquad 0^\circ < \beta < 90^\circ \tag{31}$$

and

$$\Delta Z = R + \sqrt{R^2 - \left(\frac{d}{2}\right)^2} \qquad \text{when} \qquad \beta > 90°. \tag{32}$$

From Eq. (25) we have

$$R = \frac{d}{2\sin\beta} \tag{33}$$

Hence, ΔZ can be expressed further as

$$\Delta Z_{\beta < 90°,\ \beta > 90°} = \frac{d}{2\sin\beta} \mp \sqrt{\left(\frac{d}{2\sin\beta}\right)^2 - \left(\frac{d}{2}\right)^2} = \frac{d}{2\sin\beta} \mp \frac{d}{2}\sqrt{\frac{1}{\sin^2\beta} - 1} \tag{34}$$

$$= \frac{d}{2\sin\beta} \mp \frac{d}{2}\sqrt{\frac{1-\sin^2\beta}{\sin^2\beta}} = \frac{d}{2\sin\beta} \mp \frac{d}{2}\frac{(\pm\cos\beta)}{\sin\beta} \tag{35}$$

$$= \frac{d}{2\sin\beta}\left(1 - \cos\beta\right), \tag{36}$$

where it is noted that the last expression for ΔZ is valid for β both below and above 90°. Now, by inserting Eqs. (25) and (27) into Eq. (36), ΔZ can be stated as a function of α as

$$\Delta Z(\alpha) = \frac{\left[d_0 + 2r\left(1 + \sin(\alpha - \theta_0)\right)\right]\left[1 - \cos\left(\theta_a - 90° - \alpha\right)\right]}{2\sin\left(\theta_a - 90° - \alpha\right)} \tag{37}$$

$$= -\frac{\left[d_0 + 2r\left(1 + \sin(\alpha - \theta_0)\right)\right]\left[1 - \sin\left(\theta_a - \alpha\right)\right]}{2\cos\left(\theta_a - \alpha\right)}. \tag{38}$$

With h given as in Figure 18, the sag distance measured from the top of the granule, denoted ΔZ_{top}, can be calculated according to

$$\Delta Z_{top}(\alpha) = h - r\sin\alpha - \frac{\left[d_0 + 2r\left(1 + \sin(\alpha - \theta_0)\right)\right]\left[1 - \sin\left(\theta_a - \alpha\right)\right]}{2\cos\left(\theta_a - \alpha\right)}. \tag{39}$$

By comparing ΔZ_{top} to the height of the granules (designated H), the triple line position α where a *sag transition* occurs can be determined. Finally, then, this value for

α can be inserted into Eq. (30) to find the pressure difference ΔP that is necessary for causing the sag transition. Analogous to Eq. (30) and de-pinning transitions, Eq. (39) illuminates surface features that enhances the stability against sag transitions. Especially, it is evident that a small granule separation d_0 reduces the sag distance, thereby increasing the stability against a sag transition. Thus, a small granule separation seems to make for an efficient route towards Cassie-Baxter state stability − this enhances the stability against both a de-pinning transition and a sag transition.

3.3.2. Extension of the 2D model to granules without overhangs

The model developed in the previous section can easily be extended to account for surfaces consisting of granules that do *not* exhibit re-entrant profiles. In Eqs. (30) and (39), respectively, the pressure difference ΔP and the sag distance ΔZ_{top} (measured from the top of the granule) are both functions of the triple line position α. When granules exhibit overhangs corresponding to that imaged in Figure 3, the possible values for α are seen to approximately span the range {-135°,45°} (when measuring α counter-clockwise from 3 o'clock, as before). Then, the maximum sustainable pressure difference regarding a de-pinning transition is obtained from Eq. (30) by finding the position α, within the range {-135°,45°}, where ΔP is greatest. Similarly, in Eq. (39), the possible onset of a sag transition is analyzed by determining ΔZ_{top} for each value α within the range {-135°,45°} and comparing to the granule height. Now, for a surface consisting of granules that do *not* feature overhangs, the only element that changes is *the range of possible* α. For example, if the granules exhibit straight walls, the range of possible triple line positions extends from $\alpha = 0°$ (in the direction of 3 o'clock, see Figure 18) to, say, $\alpha = 45°$ (this depends upon the shape of the top of the granule); if the granules exhibit slightly inclined walls, the range of possible triple line positions has its lower end at, say, $\alpha = 5°$ − and so on. To calculate the hydrostatic pressure that leads to a de-pinning or a sag transition, we then proceed in the exact same manner as before, using, however, another range of possible triple line positions α.

Moreover, the model can also be extended to overhangs that are *not circular* in shape. To achieve this, an individual 'overhang radius' $r(\alpha)$ needs to be assigned to each triple line position α.

In combination, these two extensions provide means for analyzing the Cassie-Baxter state stability for a wide range of granule profiles.

3.3.3. Towards a 3D model for estimating the Cassie-Baxter state stability

In addition to estimates of the Cassie-Baxter state stability against both a de-pinning and a sag transition, the two-dimensional model presented in the previous sections provides valuable physical insight into the problem. However, in the realistic three-dimensional case, the simplification of considering only *one* radius of curvature to describe the spatial distribution of the liquid-air interface is no longer valid. To determine the spatial distribution of the liquid-air interface due to a pressure difference for a general three-dimensional surface, it is required to solve the Young-Laplace equation (Eq. (16)) for all relevant points in space, using boundary conditions specific to the surface. By doing so, a three-dimensional estimate of the Cassie-Baxter state stability against both a de-pinning and a sag transition can be established. However, such calculations are difficult and requires generally numerical methods. A calculation method for this purpose has been presented by Lobaton et al. [94]. Although the study concerns pillar-structured surfaces, their proposed method can also be used for a surface consisting of overhang-shaped roughness elements. Performing such a calculation is, however, beyond the scope of this report.

3.3.4. 3D model for estimating the stability against a de-pinning transition

Still, a three-dimensional estimate of the stability against a *de-pinning transition* can be made on the basis of the direct relation between pressure difference and surface tension (Section 2.5.4). The direct relation in Eq. (22) is derived for straight-walled pillars. In that case, the vertical component of the liquid-air surface tension is always equal to $-F_{LA}\cos\theta$ (the corresponding force on the roughness element is $-LF_{LA}\cos\theta$). Conversely, on an overhang-profiled wall, the vertical component of the liquid-air surface tension varies as the triple line changes its position along the overhang (this can be seen from Figure 18; the surface tension vector points in the direction of the liquid-air interface). As a result, the vertical force on the roughness element, caused by the liquid-air interface, also changes. When the liquid-air surface tension vector, acting on the triple line, points straight down towards the bottom of the surface, this vertical force is maximized and equal to LF_{LA}. A derivation analogous to that in Section 2.5.4 then yields the following expression for the maximum sustainable pressure difference:

$$\Delta P_{max} = \frac{LF_{LA}}{(A - A_{solid})} \tag{40}$$

Eq. (40) shows that a small air pocket area $(A - A_{solid})$, or equivalently, a large solid fraction of surface, makes for a stable Cassie-Baxter state in terms of de-pinning. This can be seen as a three-dimensional version of the notion made from Eq. (30) regarding the granule separation d_0. Additionally, it is observed that a large total triple line length L stabilizes the Cassie-Baxter state. This is a feature that could not have been revealed by a two-dimensional model.

This generic approach was initially derived for straight walls (that is, not by considering an overhang), and can also be readily extended to scenarios concerning *inclined* walls. What we need for deriving a correct estimate for ΔP is the magnitude of the vertical component of the surface tension vector. As was mentioned above and can be seen from the derivation of Eq. (22) in Section 2.5.4, for straight walls this component equals $-F_{LA}\cos\theta$. If the wall is inclined by, say, an angle ϵ, the surface tension vector changes its direction accordingly (due to the fact that the intrinsic contact angle of the system stays the same). As a result, the vertical component of the surface tension vector changes its magnitude from $[-F_{LA}\cos\theta]$ to $[-F_{LA}\cos(\theta+\epsilon)]$. ΔP can then be calculated by replacing in Eq. (22) the former expression by the latter.

An approximation inherent in this approach should be mentioned. When the vertical forces acting on one roughness element is analyzed, it is assumed that the liquid-air surface tension vector points in the exact same direction everywhere along the triple line. In reality, it is likely that this direction varies somewhat.

3.3.5. Estimates of the Cassie-Baxter state stability

We are now ready to perform estimates of the stability of the Cassie-Baxter state on springtail cuticles. For that purpose, the pressure difference ΔP necessary to induce a Cassie-Wenzel transition on the different springtail cuticles has been estimated from Eqs. (30) (predicts de-pinning transition based on 2D model), (39) (predicts sag transition based on 2D model) and (40) (predicts de-pinning transition by consideration of the three-dimensional granule pattern). Experimental values for d_0, H, L, A and A_{solid} have been determined, as before, by inspection of SEM and AFM images (Figures 20-28, Appendix A). d_0 has been measured between 'diagonally' neighboring granules. The

radius r of the circular part of the overhang profile, and the distance h as shown in Figure 18, have been evaluated from the TEM image displayed in Figure 3. Using these two values for all studied springtails is clearly a coarse approximation; nevertheless, Figure 3 is currently the best available description of a re-entrant granule profile. A summary of these structural surface parameters are given in Table 4. In addition, θ_a has been assumed to be 105° as before, θ_0 has been approximated as being equal to θ_a, and a value of 0.073 N/m has been used for γ_{LA} and F_{LA} [95].

Table 4: Summary of the parameter values used in estimates of the Cassie-Baxter state stability for nine springtails.

Springtail species	d_0 [nm]	r [nm]	h [nm]	H [nm]	L [nm]	A [nm^2]	A_{solid} [nm^2]
H. viatica, SG	3000	25	25	910	2.76×10^3	2.65×10^6	0.42×10^6
I. prasis	833	25	25	62	1.60×10^3	0.92×10^6	0.16×10^6
F. quadrioculata	944	25	25	86	2.63×10^3	1.22×10^6	0.43×10^6
A. septentrionalis, SG	1379	25	25	910	4.19×10^3	4.50×10^6	1.39×10^6
A. besellsi, SG	933	25	25	93	1.16×10^3	1.04×10^6	0.06×10^6
C. clavatus	375	25	25	80	2.24×10^3	0.71×10^6	0.31×10^6
A. laricis	542	25	25	80	6.40×10^3	4.00×10^6	2.56×10^6
I. anglicana	568	25	25	80	1.89×10^3	0.66×10^6	0.22×10^6
X. maritima	944	25	25	80	2.21×10^3	1.15×10^6	0.25×10^6

Regarding the existence or absence of granule overhangs, both possibilities have been investigated when estimating the Cassie-Baxter state stability. The stability estimates for the case of absent granule overhangs have been performed by assuming straight granule walls[15]. The estimates are listed in Table 5.

Table 5 makes it clear that the Cassie-Baxter state is, indeed, very stable on springtail cuticles; for overcoming the energy barrier working against a wetting transition to the Wenzel state, hydrostatic pressures in the range $10^4 - 10^5$ Pa are required. For comparison, such a stability is 2 to 3 orders of magnitude higher than what is observed on artificial surfaces featuring micro-sized hydrophobic pillars [79]. In fact, the estimates

[15]It should be emphasized that granules exhibiting no overhangs are not necessarily straight; they may well be inclined to some degree. As discussed above, this will affect the Cassie-Baxter state stability.

Table 5: Cassie-Baxter state stability estimates for nine springtails.

	2D de-pinning transition		2D sag transition		3D de-pinning transition	
	Overhang	Straight	Overhang	Straight	Overhang	Straight
Springtail species	ΔP_{max} [Pa]	ΔP_{max} [Pa]	ΔP_{max} [Pa]	ΔP_{max} [Pa]	ΔP_{max} [Pa]	ΔP_{max} [Pa]
H. viatica (SG)	4.79×10^4	1.26×10^4	4.18×10^4	De-pins first	9.07×10^4	2.35×10^4
I. prasis	1.66×10^5	4.53×10^4	3.34×10^4	3.34×10^4	1.53×10^5	3.97×10^4
F. quadrioculata	1.47×10^5	4.00×10^4	4.00×10^4	4.00×10^4	2.44×10^5	6.32×10^4
A. septentrionalis (SG)	1.02×10^5	2.74×10^4	De-pins first	De-pins first	9.85×10^4	2.55×10^4
A. besellsi (SG)	1.49×10^5	4.04×10^4	De-pins first	De-pins first	8.66×10^4	2.24×10^4
C. clavatus	3.46×10^5	1.00×10^5	2.18×10^5	De-pins first	4.10×10^5	1.06×10^5
A. laricis	2.48×10^5	6.95×10^4	1.00×10^5	De-pins first	3.24×10^5	8.40×10^4
I. anglicana	2.37×10^5	6.63×10^4	9.16×10^4	De-pins first	3.14×10^5	8.14×10^4
X. maritima	1.47×10^5	4.00×10^4	3.47×10^4	3.47×10^4	1.79×10^5	4.65×10^4

given in Table 5 correspond well with an experimental study performed by King et al. [18] on the springtails *Anuridella marina* and *Anurida maritima*. Under submersion, these springtails were observed to be surrounded by an air film[16]. This air film disappeared when the liquid was subjected to hydrostatic pressures in the range of 5×10^4 to 2×10^5 Pa.

The 2D model and the 3D model are seen to yield quite similar estimates regarding the occurrence of a de-pinning transition. This would not have been the case if the granules displayed more intricate shapes, allowing for a significantly higher triple line length L. By use of the 3D model (Eq. (22) or Eq. (40)), we would then obtain higher stability estimates than those obtained in Table 5. On the other hand, the 2D model would produce more or less the same stability estimates as in the present case.

Furthermore, it is apparent from Table 5 that some springtails would benefit from featuring taller granules, hence making them less susceptible to sag transitions. This is especially the case if an overhang is present (column 4). However, as has been illuminated by Yu et al. [22], taller roughness structures (keeping their widths unchanged) are less stable *mechanically*. This may limit the overall advantage in growing taller granules. In fact, the results in Table 5 may be viewed as an argument for the existence a trade-off between wetting transition stability and mechanical stability; the granules are just tall enough to make the stability estimates for de-pinning transitions and sag transitions

[16]Such airfilms are referred to as 'plastrons'.

comparable.

Importantly, with stability estimates in the range of 10^4 to 10^5 Pa we can show why water droplets appear to be in a Cassie-Baxter state under goniometer contact angle measurements as reviewed in Section 3.1. In such measurements, gravity is pulling the droplet downwards. The water droplets used had volumes V of about 1 μl. This means that a gravitational force $\rho g V \sim 10^{-5}$ N was acting on the contact area between the droplet and the springtail cuticles (with $\rho = 997$ kg/m^3 being the density of water). Assuming a contact angle of $\sim 160^\circ$ (as measured) and a droplet shape corresponding to a spherical cap, the size of the contact area was approximately 1.4×10^{-7} m^2. By assuming also that the hydrostatic pressure is homogeneous over the contact area, we then obtain $\Delta P \approx 70$ Pa. This is much lower than all of the estimates for ΔP_{max}. Consequently, the appearance of a Cassie-Baxter state in a goniometer contact angle measurement is expected − the gravitational pull on the droplet is not strong enough to make the droplet transition to a Wenzel state.

Also evident from this analysis, is that an overhanging profile on the granules is *not necessary* to explain the results reviewed in Table 1; even with straight walls, the small surface protrusions represented by the granules present in itself an energy barrier against a Cassie-Wenzel transition that is much larger than the energy posed by the gravitation on a water droplet. However, if the granule height is high enough to avoid a sag transition, which is estimated to be the case for all studied springtails except *Isotomurus prasis*, *Folsomia quadrioculata* and *Xenilla maritima*, the 2D model predicts that granule overhangs can increase the Cassie-Baxter state stability by $50 - 400\%$ as compared to straight granule walls. Moreover, it should be noted that an overhang makes the Cassie-Baxter state stability much less sensitive to changes in the chemical composition of the system; indeed, if the intrinsic advancing contact angle should drop below 90°, it is seen from Eq. (22) that the stability against a Cassie-Wenzel transition vanishes completely in the case of straight walls. If overhangs are present on the granules, such a drop in the intrinsic advancing contact angle would not affect the Cassie-Baxter state stability much (*some* stability change occurs if F_{LV} becomes lower − see e.g. Eq. (40)).

We can now also estimate how far underwater springtails can maintain air pockets. Under immersion in water, a body will experience a hydrostatic pressure of $\Delta P = (\rho - \rho_{air})g\delta \approx \rho g \delta$, where δ is the immersion depth and ρ and ρ_{air} are the densities of water and air, respectively. A hydrostatic pressure of $10^4 - 10^5$ Pa is therefore equivalent

to immersion depths of

$$\delta_{lower\ bound} = \frac{10^4\ \text{Pa}}{997\ \text{kg/m}^3\ 9.81\ \text{m/s}^2} \approx 1\text{m} \tag{41}$$

$$\delta_{upper\ bound} = \frac{10^5\ \text{Pa}}{997\ \text{kg/m}^3\ 9.81\ \text{m/s}^2} \approx 10\text{m} \tag{42}$$

Based on the estimates performed in this section, it is thus indicated that springtails can maintain air pockets on their cuticles when being submerged down to water depths of $1 - 10$ m.

Moreover, a pressure of $10^4 - 10^5$ Pa is comparable to the impact of the water droplets in heavy rain [96]. Accordingly, it is possible that springtails stay dry even in this case.

We end this section with a few words regarding the differences in estimated stability across the studied species. First, we note that the (comparably) low stabilities estimated for the springtails featuring secondary granules (*Hypogastura viatica*, *Anurophorus septentrionalis* and *Archisotoma besellsi*) are probably underpredicted; it is only the stability against penetration between the *secondary* granules that has been estimated for these springtails. Due to the smaller size of their *primary* granules, a penetration through this next 'layer' is likely to require an even higher pressure. Second, we observe that the species featuring high solid fraction of surface, like *Anurophorus laricis* and *Cryptopygus clavatus*, are the ones that are estimated to display the highest stability against a Cassie-Wenzel transition. Considering that these species' low slenderness ratio[17] granules also should exhibit a high *mechanical* stability [22], this is an intriguing result.

3.4. Explaining the low contact angle hysteresis

For a surface to be water repellent, it is not only important to exhibit and maintain a high apparent contact angle, to which we have put our focus on so far. As discussed in Section 2.3, it is also essential to feature a low roll-off angle, enabled again by a low contact angle hysteresis. Table 1 shows that springtail cuticles do indeed demonstrate low CAH − in this section, we set out to understand why. As a starting point, we investigate the magnitude of CAH that would be predicted by the Choi and Dufour

[17]Defined as height divided by cross-section area.

models, reviewed in Sections 2.4.1 and 2.4.2. We will elaborate somewhat on the Dufour model, however, before we employ it.

3.4.1. CAH predictions using the Choi and Dufour models

As we saw in Section 2.4.2, the Dufour model evaluates only an indirect measure $\Delta(\cos\theta^*)$ of the CAH (Eq. (12)). In an attempt to obtain a direct measure $\Delta\theta^*$, we could expand Eq. (12) as follows:

$$\Delta(\cos\theta^*) = \frac{\Delta A}{p^2} \tag{43}$$

$$\cos\theta_r^* - \cos\theta_a^* = \frac{\Delta A}{p^2} \tag{44}$$

$$\cos\left(\overline{\theta}^* - \frac{\Delta\theta^*}{2}\right) - \cos\left(\overline{\theta}^* + \frac{\Delta\theta^*}{2}\right) = \frac{\Delta A}{p^2} \tag{45}$$

$$2\sin\left(\overline{\theta}^*\right)\sin\left(\frac{\Delta\theta^*}{2}\right) = \frac{\Delta A}{p^2} \tag{46}$$

This expression shows that $\Delta(\cos\theta^*)$, used by Reyssat and Quéré [53] and Dufour et al. [57] as a measure of CAH, is in fact not just a measure of the direct CAH ($\Delta\theta$), but also of the 'mean' apparent contact angle, defined here as $\overline{\theta}^* = \frac{\theta_a^* + \theta_r^*}{2}$. Since the mean apparent contact angle is not known *a priori*, it becomes difficult to obtain an *a priori* prediction of the CAH using this model. However, an *a posteriori* alternative is to make use of a measurement of the apparent advancing contact angle. The CAH can then be calculated according to

$$\cos(\theta_a^* - \Delta\theta^*) - \cos\theta_a^* = \frac{\Delta A}{p^2} \tag{47}$$

$$\cos(\theta_a^* - \Delta\theta^*) = \frac{\Delta A}{p^2} + \cos\theta_a^* \tag{48}$$

$$\theta_a^* - \Delta\theta^* = \arccos\left(\frac{\Delta A}{p^2} + \cos\theta_a^*\right) \tag{49}$$

$$\Delta\theta^* = \theta_a^* - \arccos\left(\frac{\Delta A}{p^2} + \cos\theta_a^*\right) \tag{50}$$

When evaluating the CAH predicted by the Dufour model, Eq. (50) will thus be used in the calculations, with θ_a^* taken as in Table 1. In addition, the deformation surface area ΔA needs to be calculated. In this report, this area will be evaluated by obtaining an analytical solution to the double integral in Eq. (14). First, however, a matter not taken into account by Reyssat and Quéré [53] or Dufour [57] is addressed: the deformation surface area, that is, the 'extra' liquid-air interface area that is generated by the presence of each defect, is equal to the area of the semi-revolved catenary curve *minus* the liquid-air interface area that would exist if there was no defect present. By inspecting Figure 13, and by considering that the apparent receding contact angle is relatively high on the surfaces that are relevant here, this liquid-air interface area will be estimated as $\frac{1}{2}\pi(p/2)^2$. This is the area of a semi-circular disk, which is equal to the area of the semi-revolved catenary curve's projection into the plane of the defect tops.

An analytical solution to the double integral in Eq. (14), which calculates the area of the semi-revolved catenary curve, can be found as follows (note that r and k are constant parameters):

$$A_{catenary} = \int_0^{\pi}\int_0^{u}\left(y(x)\sqrt{1+y'(x)^2}\right)dxd\theta \tag{51}$$

$$= \pi\int_0^{u} r\cosh\left(\frac{x-k}{r}\right)\sqrt{1+\left[\frac{d}{dx}\left(r\cosh\left(\frac{x-k}{r}\right)\right)\right]^2}dx \tag{52}$$

$$= \pi\int_0^{u} r\cosh\left(\frac{x-k}{r}\right)\sqrt{1+\sinh^2\left(\frac{x-k}{r}\right)}dx \tag{53}$$

$$= \pi\int_0^{u} r\cosh^2\left(\frac{x-k}{r}\right)dx \tag{54}$$

$$= \frac{\pi r}{4}\left[r\sinh\left(\frac{2x-2k}{r}\right)-2k+2x\right]_0^{u} \tag{55}$$

$$= \frac{\pi r}{4}\left[r\sinh\left(\frac{2u-2k}{r}\right)+2u-r\sinh\left(\frac{-2k}{r}\right)\right] \tag{56}$$

As was mentioned in Section 2.4.2, k and r can be determined from the boundary conditions $y(0) = b$ and $y'(0) = \tan\left(\frac{\pi}{2}-\tilde{\theta}\right)$. Reyssat and Quéré [53] have noted that when $\tilde{\theta} = 90°$, these two values are equal to $k = 0$ and $r = b$. Considering that the

intrinsic receding contact angle of the springtail cuticles was estimated in Section 3.2.1 to be 95°, which is quite near 90°, $k = 0$ and $r = b$ will be used in the subsequent analysis. Eq. (56) can then be expressed

$$A_{catenary} = \frac{\pi b}{4}\left[b\sinh\left(\frac{2u}{b}\right) + 2u\right] \tag{57}$$

with the maximum deformation between two defects (Eq. (15)) now given as

$$u = b\ \text{arccosh}\left(\frac{p}{2b}\right). \tag{58}$$

Then, the deformation surface area can be estimated as

$$\Delta A = A_{catenary} - \frac{1}{2}\pi\left(\frac{p}{2}\right)^2. \tag{59}$$

Now, the CAH as modelled by the Dufour model can be evaluated from Eqs. (50), (57), (58) and (59) by employing experimentally obtained values for b, p and θ_a^*. These values, together with the parameters f_a and f_r, which are required to predict CAH by use of the Choi model (Eqs. (10) and (11)), have been determined for the springtails shown in Figures 20-28 (Appendix A) and are summarized in Table 6. Identical to what Choi et al. [62] assumed for their surfaces consisting of 'discrete hoodoos', f_a is assumed here to be zero (no solid fraction experienced by the advancing edge of the contact line). Table 6 also lists the CAH as predicted by the Choi and Dufour models and the CAH that was determined experimentally.

An obvious result observed in Table 6 is the inability of the Choi model to predict the CAH measured on the springtail cuticles. Indeed, the CAH modelled by Choi et al. is significantly overpredicted for all the springtails that are studied here. Even if assuming (as Choi et al. did) that vibrational perturbations from the laboratory environment are responsible for observing advancing apparent contact angles somewhat lower than 180°, CAH is still overpredicted. For the springtail cuticles that exhibit large solid fraction of surface, leading to a high value for f_r, the overprediction is especially severe (e.g., *C. clavatus* and *A. laricis*). Considering that the Choi model has been successful in predicting the CAH on micro-structured surfaces [57, 62], the lack of success

Table 6: Predicted and measured contact angle hysteresis on springtail cuticles. Note that the Dufour model does not predict advancing apparent contact angles – the values in column 10 are collected from the experimental values listed in column 13.

					Choi model			Dufour model			Measured		
Springtail species	b [nm]	p [nm]	f_r	f_a	θ_r [°]	θ_a [°]	$\Delta\theta$ [°]	θ_r [°]	θ_a [°]	$\Delta\theta$ [°]	θ_r [°]	θ_a [°]	$\Delta\theta$ [°]
H. viatica, SG	285	2850	0.20	0	146.6	180	33.4	161.8	167.9	6.1	163.2	167.9	4.7
I. prasis	207.5	1285	0.32	0	137.4	180	42.6	157.9	168.2	10.3	164.1	168.2	4.1
F. quadrioculata	302.5	1210	0.50	0	125.9	180	54.1	155.6	171.0	15.4	166.5	171.0	4.5
A. septentrionalis, SG	572.5	2430	0.47	0	127.7	180	52.3	154.8	168.3	13.5	164.8	168.3	3.5
A. besellsi, SG	135	865	0.31	0	138.1	180	41.9	158.9	169.6	10.7	164.5	169.6	5.0
C. clavatus	390	975	0.80	0	109.8	180	70.2	162.4	166.0	3.6	166.2	166.0	-0.2
A. laricis	765	1880	0.81	0	109.3	180	70.7	156.2	157.4	1.2	161.2	157.4	-3.9
I. anglicana	245	780	0.63	0	118.6	180	61.4	145.8	154.3	8.5	158.6	154.3	-4.3
X. maritima	260	915	0.57	0	121.9	180	58.1	148.6	158.7	10.1	132.4	158.7	26.3

in predicting CAH on the springtail cuticles is noteworthy. In the light of this finding, a recent experimental study by Dorrer et al. [97] becomes interesting for our cause. In that study, microstructured surfaces were fabricated in such a way that the post widths were varied while other surface characteristics were kept unchanged. As shown in Figure 19, it was found that decreasing the post width also decreased the CAH. In other words, the sheer size of the roughness features on a composite surface seems to be playing a role in determining the CAH exhibited by the surface.

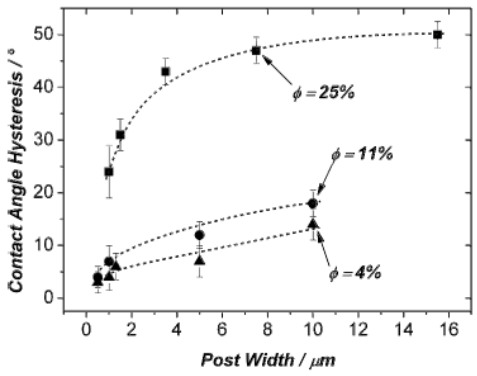

Figure 19: CAH measured on fluoropolymer-coated silicon posts of different widths, in a study by Dorrer et al [97]. ϕ denotes the solid fraction of surface (we have used f for this value). The dashed lines are meant as guides to the eye.

In the study by Dorrer et al., the measured CAH decreased significantly as the micropost widths decreased from tens of micrometers down to $\sim$1 μm (Figure 19). By comparison, the granules on the springtail cuticles have widths $2b$ ranging from 0.27 to 1.53 μm − a defect size interval ranging even below that investigated by Dorrer et al. One may thus speculate, that the small size of the granules is a key point for understanding the low CAH observed for the springtails.

Dorrer et al. hypothesized that their results could be explained by considering that droplets detach sequentially from each defect, and that the energy barriers involved in detaching from small defects are lower than those involved for larger defects. As a result, CAH would be lowered for smaller defect widths. Recently, an experimental study by Dufour et al. [98] observed exactly such a sequential droplet detaching on a microstructured surface − hence giving support to such a theory. However, if this was the whole story to CAH, one would expect a clear relationship between the springtail cuticle's defect widths and their measured CAH values. Such a clear relationship is not tractable in Table 6. An explanation for this may lie in the fact that both adhesion hysteresis and defect pinning are expected to contribute to CAH, and in that their dependence upon defect width may prove to be different. Being a mechanism that involves interactions between liquid and solid, the contribution of *adhesion hysteresis* to CAH is thought to be proportional to the solid-liquid interfacial area [6]. Thus, as defects become smaller, it seems well-grounded that the energy barriers relating to adhesion hysteresis should decrease. In line with this reasoning, the contribution of adhesion hysteresis to CAH should vanish as the defect widths become sufficiently small (assuming, still, a sequential droplet detaching). On the other hand, the relationship between defect width and *defect pinning* may be more complex. Consider for example Figure 11c. Although the droplet detaches from each defect sequentially, the deformed liquid-air interfaces involved at each defect are seen to be built up simultaneously. As a result, while the energy barriers resulting from adhesion hysteresis, and hence its contribution to CAH, may vanish for sufficiently small defects, the energy barriers relating to defect pinning may perhaps not. Hence, one may speculate that the CAH measured in Table 6 is dominated by defect pinning, and not by adhesion hysteresis. This could explain why no clear relationship between CAH and defect width is observed for the springtail cuticles.

In the Dufour model, it is exactly the defect pinning contribution to CAH that is considered. The CAH predictions by use of this approach are shown in the eleventh column of Table 6. It is evident that the CAH predictions are generally relatively

low, almost as low as the CAH that is observed experimentally (column $12-14$ in Table 6). This could reflect the fact that this model contains no contribution from adhesion hysteresis. However, the predictions are not very accurate. This can perhaps be explained by the approximations made in the model. As is noted by Dufour et al. [57], for an accurate computation of the CAH, the liquid-air deformation surface area should be modelled by a more complex function than what is used here − a more accurate function should take into account, for instance, that the local receding contact angle $\tilde{\theta}$ varies along the defect perimeter (see for instance, Figure 11b). Moreover, it is not certain that the deformed liquid-air interface takes on a shape well described by a semi-revolved catenary curve (Figure 13) for every combination of defect size and defect separation. Especially, one may question the assumption that the triple line settles on the surface in the same way for a nanostructured surface as it does for a microstructured surface. Still, an interesting notion from the eleventh column in Table 6, is that the springtails with the highest f_r, that is, those with the highest solid fraction of surface as experienced by the receding edge of the triple line, are predicted to show the lowest CAH (*C. clavatus* and *A. laricis*). A low CAH for these springtails is also what is observed. It can thus be hypothesized that the Dufour model captures a phenomenon where high solid fraction of surface leads to a low contribution to CAH from defect pinning, due to a less deformed liquid-air interface.

3.4.2. Incorporating line tension into the Choi model

Neither the Choi model nor the Dufour model is able to predict a size effect concerning the defects on a surface and the CAH observed on the surface − both models are scale-independent. With the objective of obtaining a scale-dependent model, one can argue that in the same manner as Zheng et al. [25] modified the Cassie-Baxter equation to incorporate the contribution of *line tension*, so too should the differential Cassie equations by Choi et al. (Eqs. (10) and (11)) be modified. Doing so leads to the following 'modified Choi equations':

$$\cos\theta_a^* = -1 + f_a\left(r_f\cos\theta + 1 - \frac{\lambda}{S_a\gamma_{LV}}\right) \tag{60}$$

$$\cos\theta_r^* = -1 + f_r\left(r_f\cos\theta + 1 - \frac{\lambda}{S_r\gamma_{LV}}\right). \tag{61}$$

In Eqs. (60) and (61), S_a and S_r refer, by analogy to f_a and f_r, to the 'differential' roughness scale at the advancing and receding edge of a droplet. Just like the Zheng equation (Eq. (7)) predicts that the apparent contact angle of a droplet depends on the roughness scale S of the solid features of a surface, Eqs. (60) and (61) predict that the CAH of a surface depends on the roughness scales S_a and S_r at the advancing and receding edges of the droplet. This modification thus has the potential to explain why surfaces otherwise equivalent, can exhibit lower CAH as the scale of the solid features decreases.

To quantitatively evaluate the magnitude of these differential roughness scales for surfaces consisting of discrete granules (or discrete posts, for that matter), the change in line energy involved in small displacements of the contact line at the advancing and receding edges of the droplet should be considered. For a small displacement of the contact line at the advancing edge (Figure 10a), from the outer edge of one array of granules to the next array of granules, no solid surface is traversed and no total triple line length is added nor subtracted. In this case, there is no change in line energy, and no modification to the original Choi equation for the advancing droplet edge (Eq. (10)) is necessary. On the other hand, if assuming, as Choi et al. [62], that the contact line at the receding edge is bridging between the granules as in Figure 10b, a small displacement of the contact line at this edge will indeed involve changes in total triple line length. For a small displacement ϵ at the receding edge of the droplet, the solid surface area traversed for each granule is equal to $2W\epsilon$. At the same time, a triple line length of 2ϵ is traversed for each granule (Figure 10b). Consequently, the receding differential roughness scale is equal to

$$S_r = \frac{A_r}{L_r} = \frac{2W\epsilon}{2\epsilon} = W. \tag{62}$$

For surfaces consisting of granules or posts, the modified Choi equations can thus be written as

$$\cos\theta_a^* = -1 + f_a\left(r_f \cos\theta + 1\right) \tag{63}$$

$$\cos\theta_r^* = -1 + f_r\left(r_f \cos\theta + 1 - \frac{\lambda}{W\gamma_{LV}}\right). \tag{64}$$

To analyze whether Eqs. (63) and (64) can explain the low CAH observed on springtails, we use Eq. (64) to calculate the line tension magnitude λ necessary to yield a receding apparent contact angle prediction identical to that observed[18]. Regarding the calculations, it has been noted that W in Figure 10 and b in Figure 12 both denote the half-width of one defect − hence, $W = b$. Moreover, θ and r_f have again been approximated as 100° and 1, respectively. The results of the calculations are presented in Table 7, which also lists the parameters used and the advancing apparent contact angles predicted from Eq. (63) (these are identical to those predicted in Table 6 by using Eq. (10), but are included here for completeness).

Table 7: Line tension magnitude (λ) required to explain the receding apparent contact angle (θ_r^*) measured on nine springtails, using a 'modified Choi model' (Eq. (64)).

				Measured		Modified Choi model		
Springtail species	$S_r = W = b$ [nm]	f_r	f_a	θ_r^* [°]	θ_a^* [°]	θ_r^* [°]	θ_a^* [°]	λ [J/m]
H. viatica (SG)	285	0.20	0	163.2	167.9	163.2	180	1.28×10^{-8}
I. prasis	207.5	0.32	0	164.1	168.2	164.1	180	1.07×10^{-8}
F. quadrioculata	302.5	0.50	0	166.5	171.0	166.5	180	1.70×10^{-8}
A. septentrionalis (SG)	572.5	0.47	0	164.8	168.3	164.8	180	3.14×10^{-8}
A. besellsi (SG)	135	0.31	0	164.5	169.6	164.5	180	6.99×10^{-9}
C. clavatus	390	0.80	0	166.2	166.0	166.2	180	2.25×10^{-8}
A. laricis	765	0.81	0	161.2	157.4	161.2	180	4.25×10^{-8}
I. anglicana	245	0.63	0	158.6	154.3	158.6	180	1.28×10^{-8}
X. maritima	260	0.57	0	132.4	158.7	132.4	180	4.84×10^{-9}

Notably, Table 7 shows that incorporation of line tension into the Choi equations may indeed explain the low CAH seen for the springtail cuticles, given that the line tension magnitude is of the order of 10^{-8} J/m. This line tension magnitude is similar to that found in Section 3.2.3. The measurements on *A. besellsi* and *X. maritima* predict

[18]Since Eq. (63) yields $\theta_a^* = 180°$ for springtails, a value that may be shadowed by vibrational perturbations in the laboratory, we parametrize λ by using measurements of the receding apparent contact angle θ_r^*, and not the measured contact angle hysteresis. However, it *may* be the case that also the *receding* apparent contact angle measurements are affected by vibrational perturbations.

somewhat lower line tension magnitudes, however. *X. maritima* will be discussed in more detail in Section 3.4.3.

It is interesting that in the review "Contact Angle Hysteresis Explained" [43], Gao and McCarthy predict that surfaces with a high degree of 'contact line tortuosity' will exhibit a low contact angle hysteresis, due to increased ground-state energies of the droplet and thereby decreased activation barriers between metastable states. The incorporation of line tension into the Choi model, giving rise to an increased apparent contact angle at the receding edge of a droplet's perimeter, is a quantification of such an argument.

Line tension can also help explain an experimental finding by Öner and McCarthy [99]. They found that changing the shape of the pillars on a microstructured surface, from square to staggered rhombus, star, or indented square, caused increases in the apparent receding contact angle. In the light of Eq. (61), this can be understood as follows: as the pillar shape changes from square to more complex shapes, L_r increases relative to A_r. Hence S_r decreases, which from Eq. (61) translates into an increased receding contact angle.

3.4.3. The relatively high CAH observed on X. maritima

In contrast to the other springtail species studied in this report, *X. maritima* does not show a very low CAH (26.3°, Table 1). By inspecting Figure 28 (Appendix A), a qualitative argument for this observation can be made on the basis of the above discussion. Figure 28 shows that the cuticle of *X. maritima* contains numerous 'microfolds' − it has a corrugated appearance on the micrometer scale. When a water droplet sits on this surface, it will perhaps not penetrate between every microfold. Thus, in effect, the water droplet is sitting on larger defects. This has the consequence of leading to *less* total line length involved at the receding edge of the droplet. In Eq. (61), this results in a higher S_r and hence a lower receding contact angle. At the same time, since the droplet is still sitting on (now, micro-sized) defects, the advancing contact angle will be large because the advancing differential solid fraction parameter f_a is low (Eq. (60)). In combination, this could result in a considerable CAH.

3.5. The springtail's design strategy for achieving robust water repellency

The analysis performed in this report indicates that springtails utilize a simple and elegant design principle for enabling a robust water repellent behavior − namely, by sculpturing its surface with roughness features of just the right size.

When the roughness asperities of a surface have widths of a few microns or more, it is evident from Eqs. (4), (10) and (11) that the only way to ensure high apparent contact angles and low contact angle hysteresis is to exhibit a very small solid fraction of surface (f). However, given asperity widths of a few microns or more, a very small solid fraction of surface corresponds to 'large' separations between the asperities; in Section 3.3 we saw that this renders the Cassie-Baxter state unstable. Moreover, the mechanical stability of sparsely distributed asperities (low f) will be low, unless the asperities are very short [22]. On the other hand, if the asperities are short, the proneness to sag transitions will be high (Eq. (39)), again lowering the stability of the Cassie-Baxter state. As such, a combination of high apparent contact angles, low contact angle hysteresis, high Cassie-Baxter state stability and high mechanical stability seems to be physically impossible if the roughness elements of a surface have widths of a few microns or more.

However, if the roughness asperity widths become small enough (sub-micron to micron size scale), we have seen that it is possible − mediated, perhaps, by the mechanisms of line tension and diminished adhesion hysteresis energy barriers − to achieve both high apparent contact angles and low contact angle hysteresis, *regardless* of the magnitude of solid fraction of surface. As a result, it becomes possible to obtain both mechanical robustness and a stable Cassie-Baxter state, by increasing the solid fraction of surface, *without* lowering the apparent contact angles or escalating the contact angle hysteresis. The cuticles of *A. laricis* and *C. clavatus* are illustrative examples of this simple, yet effective design strategy for obtaining a robust water repellency.

We could also ask: wouldn't it be desirable − for achieving even better water repellent properties − to downsize the roughness elements even further, from the sub-micrometer scale down to the 'true' nanometer scale (below ∼100 nm)? From the analysis brought about in this work, the answer is yes. However, experiments suggest that there exists also a *lower limit*, somewhere in the nanometer scale, where a continued roughness element downsizing will lead to a marked *increase* in contact angle hysteresis [100] − this is seen, for instance, in the superhydrophobic, yet highly adhesive 'Petal Effect' observed on rose

petals [101, 102]. In other words, for achieving robust water repellent properties, the roughness elements of a surface should not be *too* small, either − rather, there exists an optimum size range, in which the roughness elements' widths should lie. The granules on springtail cuticles provide natural examples of such elements.

4. Conclusions and outlook

In this study, we have performed a quantitative analysis of the wetting properties of springtail cuticles. We have based our discussion on a set of contact angle measurements on nine different springtail species, revealing that springtail cuticles generally show high apparent contact angles and low contact angle hysteresis. It turned out, that an understanding of the measured high apparent contact angles requires us to assume that water exists in a Cassie-Baxter wetting state. Furthermore, the effect of three-phase line tension has to be taken into account. The importance of line tension in determining the apparent contact angle is due to the large total triple line length that exists when water is situated on small roughness features − the micron to sub-micron size scale of the granule pattern is thus essential to the springtails for achieving such high apparent contact angles. The line tension's magnitude needs to be of the order of 10^{-8} J/m to explain the experimental findings, which is a magnitude that corresponds well to values reported in the literature [41].

However, a Wenzel wetting state is found to be energetically favorable compared to the Cassie-Baxter wetting state. Water seems therefore to exist in a *metastable* Cassie-Baxter state on the springtail cuticles, experiencing an energy barrier against transitioning from the Cassie-Baxter state to a lower energy Wenzel state. By developing and employing a two-dimensional model, it is shown that the granules on the springtail cuticles present such an energy barrier. Numerical estimates based on the model indicate that the Cassie-Baxter state is stable against hydrostatic pressures up to $10^4 - 10^5$ Pa. Interestingly, the existence of overhangs on the granules is not necessary to predict an energy barrier inhibiting water from transitioning from a Cassie-Baxter state to a Wenzel state. Yet, arguments are put forth viewing that overhangs make the stability of the Cassie-Baxter state less sensitive to changes in the system's chemical composition. In addition, they are estimated to increase the stability of the Cassie-Baxter state by $50 - 400\%$ as compared to granules featuring straight walls. Other factors suggested to contribute to a high stability of the Cassie-Baxter state, are short granule separations, a high solid fraction of surface, a large total triple line length and tall granules.

The low contact angle hysteresis observed on springtail cuticles can not be understood from the quantitative CAH models that currently exist in the literature. It is argued, however, that the small size of the granules is relevant also in this respect − a droplet needs to overcome only a low adhesion hysteresis energy barrier, in order to detach from

a small granule, enabling droplet motion. By incorporating three-phase line tension into a recent CAH model for composite surfaces [62], new equations for determining CAH on composite surfaces are proposed. If assuming, as before, a line tension magnitude of the order of 10^{-8} J/m, these equations successfully describe the low CAH on springtail cuticles.

In summary, the sub-micron size scale of the granules is found to be the most essential factor for rendering the springtail cuticles water repellent.

Several lines of research can be envisaged for achieving a more comprehensible understanding of the wetting properties observed on springtail cuticles. Considering the importance of the three-phase line tension in describing apparent contact angles and possibly also contact angle hysteresis, studies illuminating the line tension's nature would be desirable. For example, does curvature of the triple line affect its magnitude? How is it dependent upon the nature of the phases that are meeting at the triple line? Perhaps might molecular modelling studies be suited for answering such questions.

Ubiquitous in the analysis presented here are the assumptions regarding the intrinsic contact angles on the springtail cuticle. Thus, the accuracy of this analysis would improve if these assumptions were examined experimentally. A possibility might be to extract the seemingly apparent top wax layer from the springtail cuticles, distribute it on a smooth surface and subsequently perform contact angle measurements.

From a theoretical viewpoint, the potential role of *hairs* in determining the wetting properties of springtails could be studied more thoroughly than what is done in this report. Moreover, for a more precise estimate of the Cassie-Baxter state stability against sag transitions, numerical methods could be employed to reveal how the liquid-air interface responds to a given hydrostatic pressure. It would also be interesting to evaluate the Cassie-Baxter state stability experimentally. This could be achieved by performing immersion experiments or experiments using impacting droplets. Such experiments might also shed light over the proposed link between granule overhangs and increased Cassie-Baxter state stability.

SEM inspection of curable polymer droplets presents an exciting approach for surfaces able to sustain liquids with low surface tension in a Cassie-Baxter state [62, 57] − springtail cuticles featuring granules with overhangs should be capable in this respect. Such studies could be used for gaining information about the liquid-air interface deformation areas that arise when the cuticle − or, if experimentally more feasible, artificial

surfaces *modelling* the cuticle − is tilted. This, in turn, could give clues for a better understanding of the low CAH observed on the cuticles. Another means of increasing the understanding of CAH on springtails, would be to assess the validity of the novel equations incorporating line tension into the Choi model (Section 3.4.2). Such an assessment should be viable by fabricating and performing contact angle measurements on a set of surfaces comprising different triple line lengths, but that are otherwise equivalent.

For springtail-inspired surfaces to be employed technologically, a high degree of durability and wear resistance is required. In this light, a more thorough evaluation of the *mechanical properties* of the springtail cuticles is imperative. Both experimental and theoretical endeavours would come in hand for that purpose.

In this study, the species *Anurophorus laricis* and *Cryptopygus clavatus* have emerged as promising candidates for inspiring man-made springtail cuticle replicas − their combination of high solid fraction of surface and small granule sizes equip them with outstanding water repellent properties. Additionally, they should possess relatively good mechanical properties. Fabrication and assessment of surfaces mimicking these species' cuticles present exciting possibilities for future studies.

References

[1] Guo, Z., Liu, W., Su, B.-L.
"Superhydrophobic surfaces: From natural to biomimetic to functional"
Journal of Colloid and Interface Science, **353**, 2011, 335-355.

[2] Barthlott, W. and Neinhuis, C.
"Purity of the sacred lotus, or escape from contamination in biological surfaces"
Planta, **202**, 1997, 1-8.

[3] Neinhuis, C. and Barthlott, W.
"Characterization and Distribution of Water-repellent, Self-cleaning Plant Surfaces"
Annals of Botany, **79**, 1997, 667-677.

[4] Koch K., Bhushan, B., Barthlott, W.
"Multifunctional surface structures of plants: An inspiration for biomimetics"
Progress in Materials Science, **54**, 2009, 137-178.

[5] Oeffner, J. and Lauder, G. V.
"The hydrodynamic function of shark skin and two biomimetic applications"
Journal of Experimental Biology **215**, 2012, 785-795.

[6] Bhushan, B. and Jung, Y. C.
"Natural and biomimetic artificial surfaces for superhydrophobicity, self-cleaning, low adhesion, and drag reduction"
Progress in Materials Science, **56**, 2011, 1-108.

[7] Feng, X.-Q., Gao, X., Wu, Z., Jiang, L., Zheng, Q.-S.
"Superior Water Repellency of Water Strider Legs with Hierarchical Structures: Experiments and Analysis"
Langmuir, **23**, 2007, 4892-4896.

[8] Onda, T., Shibuichi, S., Satoh, N., Tsujii, K.
"Super-Water-Repellent Fractal Surfaces"
Langmuir, **12(9)**, 1996, 2125-2127.

[9] Gao, L., McCarthy, T. J., Zhang, X.
"Wetting and Superhydrophobicity"
Langmuir, **25(24)**, 2009, 14100-14104.

[10] Nosonovsky, M. and Bhushan, B.
"Superhydrophobic surfaces and emerging applications: Non-adhesion, energy, green engineering"
Current Opinion in Colloid & Interface Science, **14**, 2009, 270-280.

[11] Bhushan, B.
"Biomimetics inspired surfaces for drag reduction and oleophobicity/philicity"
Beilstein Journal of Nanotechnology, **2**, 2011, 66-84.

[12] Feng, L., Li, S., Li, Y., Li, H., Zhang, L., Zhai, J., Song, Y., Liu, B., Jiang, L., Zhu, D.
"Super-Hydrophobic Surfaces: From Natural to Artificial"
Advanced Materials, **14(24)**, 2002, 1857-1860.

[13] Sun, T., Feng, L., Gao, X., Jiang, L.
"Bioinspired Surfaces with Special Wettability"
Accounts of Chemical Research, **38**, 2005, 644-652.

[14] Shirtcliffe, N. J., McHale, G., Atherton, S., Newton, M. I.
"An introduction to superhydrophobicity"
Advances in Colloid and Interface Science, **161**, 2010, 124-138.

[15] Noble-Nesbitt, J.
"Transpiration in *Podura aquatica l.* (Collembola, Isotomidae) and the Wetting Properties of its Cuticle"
Journal of Experimental Biology, **40**, 1963, 681-700.

[16] Gillott, C.
"Entomology"
Springer, 2005, pp. 113-126.

[17] Ghiradella, H. and Radigan, W.
"Collembolan Cuticle: Wax Layer and Anti-Wetting Properties"
Journal of Insect Physiology, **20**, 1974, 301-306.

[18] King, P. E., Pugh, P. J. A., Fordy, M. R., Love, N., Wheeler, S. A.
"A comparison of some environmental adaptations of the littoral collembolans *Anuridella marina* (Willem) and *Anurida maritima* (Guérin)"
Journal of Natural History, **24**, 1990, 673-688.

[19] Helbig, R., Nickerl, J., Neinhuis, C., Werner, C.
"Smart Skin Patterns Protect Springtails"
PLoS ONE, **6(9)**, 2011, e25105.

[20] Patankar, N. A.
"Mimicking the Lotus Effect: Influence of Double Roughness Structures and Slender Pillars"
Langmuir, **20**, 2004, 8209-8213.

[21] Gao, L. and McCarthy, T. J.
"The 'Lotus Effect' Explained: Two Reasons Why Two Length Scales of Topography Are Important"
Langmuir, **22**, 2006, 2966-2967.

[22] Yu, Y., Zhao, Z.-H., Zheng, Q.-S.
"Mechanical and Superhydrophobic Stabilities of Two-Scale Surfacial Structure of Lotus Leaves"
Langmuir, **23**, 2007, 8212-8216.

[23] Gao, H., Wang, X., Yao, H., Gorb, S., Arzt, E.
"Mechanics of hierarchical adhesion structures of geckos"
Mechanics of Materials, **37**, 2005, 275-285.

[24] Cranford, S. W., Tarakanova, A., Pugno, N. M., Buehler, M. J.
"Nonlinear material behaviour of spider silk yields robust webs"
Nature, **482**, 2012, 72-76.

[25] Zheng, Q.-S., Lv, C.-J., Hao, P.-F., Sheridan, J.
"Small is beautiful, and dry"
Science China Physics, Mechanics & Astronomy, **53(12)**, 2010, 2245-2259.

[26] Young, T.
"An Essay on the Cohesion of Fluids"
Philosophical Transactions of the Royal Society of London, **95**, 1805, 65-87.

[27] de Gennes, P.-G., Brochard-Wyart, F., Quéré, D.
"Capillarity and Wetting Phenomena: Drops, Bubbles, Pearls, Waves"
Springer-Verlag New York, Inc. 2004.

[28] Gao, L. and McCarthy, T. J.
"Wetting 101°"
Langmuir, **25(24)**, 2009, 14105-14115.

[29] Luo, C., Xiang, M., Liu, X., Wang, H.
"Transition from Cassie-Baxter to Wenzel States on microline-formed PDMS surfaces induced by evaporation or pressing of water droplets"
Microfluid Nanofluid, **10**, 2011, 831-842.

[30] Wenzel, R. N.
"Resistance of Solid Surfaces to Wetting by Water"
Industrial and Engineering Chemistry, **28(8)**, 1936, 988-994.

[31] Marmur, A.
"Wetting on Hydrophobic Rough Surfaces: To Be Heterogeneous or Not To Be?"
Langmuir, **19**, 2003, 8343-8348.

[32] Cassie, A. B. D. and Baxter, S.
"Wettability of porous surfaces" ta en sjekk på dette!
Trans. Faraday Soc., **40**, 1944, 546-551.

[33] Gao, L. and McCarthy, T. J.
"How Wenzel and Cassie Were Wrong"
Langmuir, **23**, 2007, 3762-3765.

[34] Panchagnula, M. V. and Vedantam, S.
"Comment on How Wenzel and Cassie Were Wrong by Gao and McCarthy"
Langmuir, **23**, 2007, 13242-13242.

[35] McHale, G.
"Cassie and Wenzel: Were They Really So Wrong?"
Langmuir, **23**, 2007, 8200-8205.

[36] Nosonovsky, M.
"On the Range of Applicability of the Wenzel and Cassie Equations"
Langmuir, **23**, 2007, 9919-9920.

[37] Whyman, G., Bormashenko, E., Stein, T.
"The rigorous derivation of Young, Cassie-Baxter and Wenzel equations and the analysis of the contact angle hysteresis phenomenon"
Chemical Physics Letters, **450**, 2008, 355-359.

[38] Marmur, A. and Bittoun, E.
"When Wenzel and Cassie Are Right: Reconciling Local and Global Considerations"
Langmuir, **25**, 2009, 1277-1281.

[39] Erbil, H. Y. and Cansoy, C. E.
"Range of Applicability of the Wenzel and Cassie-Baxter Equations for Superhydrophobic Surfaces"
Langmuir, **25(24)**, 2009, 14135-14145.

[40] Kwon, Y., Choi, S., Anantharaju, N., Lee, J., Panchagnula, M. V., Patankar, N. A.
"Is the Cassie-Baxter Formula Relevant?"
Langmuir, **26(22)**, 2010, 17528-17531.

[41] Amirfazli, A. and Neumann, A. W.
"Status of the three-phase line tension"
Advances in Colloid and Interface Science, **110**, 2004, 121-141.

[42] Quéré, D.
"Non-sticking drops"
Rep. Prog. Phys., **68**, 2005, 2495-2532.

[43] Gao, L. and McCarthy, T. J.
"Contact Angle Hysteresis Explained"
Langmuir, **22**, 2006, 6234-6237.

[44] Bormashenko, E., Bormashenko, Y., Whyman, G., Pogreb, R, Musin, A., Jager, R., Barkay, Z.
"Contact Angle Hysteresis on Polymer Substrates Established with Various Experimental Techniques, Its Interpretation, and Quantitative Characterization"
Langmuir, **24**, 2008, 4020-4025.

[45] Marmur, A.
"Solid-Surface Characterization by Wetting"
Annu. Rev. Mater. Res, **39**, 2009, 473-489.

[46] Vedantam, S. and Panchagnula, M. V.
"Constitutive modeling of contact angle hysteresis"
Journal of Colloid and Interface Science, **321**, 2008, 393-400.

[47] Xu, X. and Wang, X.
"Analysis of Wetting and Contact Angle Hysteresis on Chemically Patterned Surfaces"
Siam J. Appl. Math, **71(5)**, 2011, 1753-1779.

[48] Wu, C.-D., Kuo, L.-M., Lin, S.-J., Fang, T.-H., Hsieh, S.-F.
"Effects of temperature, size of water droplets, and surface roughness on nanowetting properties investigated using molecular dynamics simulation"
Computational Materials Science, **53**, 2012, 25-30.

[49] Jeong, W.-J., Ha, M. Y., Yoon, H. S., Ambrosia, M.
"Dynamic Behavior of Water Droplets on Solid Surfaces with Pillar-Type Nanostructures"
Langmuir, **28**, 2012, 5360-5371.

[50] Kusumaatmaja, H. and Yeomans, J. M.
"Modeling Contact Angle Hysteresis on Chemically Patterned and Superhydrophobic Surfaces"
Langmuir, **23**, 2007, 6019-6032.

[51] Mognetti, B. M. and Yeomans, J. M.
"Modeling Receding Contact Lines on Superhydrophobic Surfaces"
Langmuir, **26(23)**, 2010, 18162-18168.

[52] Extrand, C. W.
"Model for Contact Angles and Hysteresis on Rough and Ultraphobic Surfaces"
Langmuir, **18**, 2002, 7991-7999.

[53] Reyssat, M. and Quéré, D.
"Contact Angle Hysteresis Generated by Strong Dilute Defects"
J. Phys. Chem. B, **113**, 2009, 3906-3909.

[54] Lv, C, Yang, C., Hao, P., He, F., Zheng, Q.
"Sliding of Water Droplets on Microstructured Hydrophobic Surfaces"
Langmuir, **26(11)**, 2010, 8704-8708.

[55] Santos, M. J. and White, J. A.
"Theory and Simulation of Angular Hysteresis on Planar Surfaces"
Langmuir, **27**, 2011, 14868-14875.

[56] Debuisson, D., Senez, V., Arscott, S.
"Tunable contact angle hysteresis by micropatterning surfaces"
Applied Physics Letters, **98**, 2011, 184101.

[57] Dufour, R., Harnois, M., Thomy, V., Boukherroub, R., Senez, V.
"Contact angle hysteresis origins: Investigation on super-omniphobic surfaces"
Soft Matter, **7**, 2011, 9380-9387.

[58] Long, J. and Chen, P.
"On the role of energy barriers in determining contact angle hysteresis"
Adv. Colloid Interface Sci., **127**, 2006, 55-66.

[59] Li, W. and Amirfazli, A.
"Microtextured superhydrophobic surfaces: A thermodynamic analysis"
Adv. Colloid Interface Sci., **132**, 2007, 51-68.

[60] Yamamoto, K. and Ogata, S.
"3-D thermodynamic analysis of superhydrophobic surfaces"
Journal of Colloid and Interface Science, **326**, 2008, 471-477.

[61] Rodriguez-Valverde, M. A., Montes Ruiz-Cabello, F. J., Cabrerizo-Vilchez, M. A.
"Wetting on axially-patterned heterogeneous surfaces"
Adv. Colloid Interface Sci., **138**, 2008, 84-100.

[62] Choi, W., Tuteja, A., Mabry, J. M., Cohen, R. E., McKinley, G. H.
"A modified Cassie-Baxter relationship to explain contact angle hysteresis and anisotropy on non-wetting textured surfaces"
Journal of Colloid and Interface Science, **339**, 2009, 208-216.

[63] Zhang, H., Li, W., Fang, G.
"A new model for thermodynamic analysis on wetting behavior of superhydrophobic surfaces"
Applied Surface Science, **258**, 2012, 2707-2716.

[64] Yu, Y., Wu, Q., Zhang, K, Ji, B.
"Effect of triple-phase contact line on contact angle hysteresis"
Science China Physics, Mechanics & Astronomy, **55**, 2012, 1-6.

[65] Hong, S.-J., Chou, T.-H., Chan, S. H., Sheng, Y.-J., Tsao, H.-K.
"Droplet Compression and Relaxation by a Superhydrophobic Surface: Contact Angle Hysteresis"
Langmuir, **28(13)**, 2012, 5606-5613.

[66] Israelachvili, J. N.
"Intermolecular and Surface Forces"
Academic Press: New York, 1985.

[67] Hong, S.-J., Chang, F.-M., Chou, T.-H., Chan, S. H., Sheng, Y.-J., Tsao, H.-K.
"Anomalous Contact Angle Hysteresis of a Captive Bubble: Advancing Contact Line Pinning"
Langmuir, **27**, 2011, 6890-6896.

[68] Cassie, A. B. D.
"Contact Angles"
Discussions of the Faraday Society, **3**, 1948, 11-16.

[69] Joanny, J. F. and de Gennes, P. G.
"A model for contact angle hysteresis"
J. Chem. Phys., **81**, 1984, 552-562.

[70] Furmidge, C. G. L.
"Studies at phase interfaces. I. The sliding of liquid drops on solid surfaces and a theory for spray retention"
Journal of Colloid Science, **17**, 1962, 309-324.

[71] Nosonovsky, M. and Bhushan, B.
"Green Tribology: Biomimetics, Energy Conservation and Sustainability"
Springer-Verlag Berlin Heidelberg, 2012, pp. 127-147.

[72] Lafuma, A. and Quéré, D.
"Superhydrophobic states"
Nature Materials, **2**, 2003, 457-460.

[73] Bormashenko, E., Stein, T., Whyman, G., Bormashenko, Y., Pogreb, R.
"Wetting properties of the multiscaled nanostructured polymer and metallic superhydrophobic surfaces"
Langmuir, **22**, 2006, 9982-9985.

[74] Patankar, N. A.
"Transition between Superhydrophobic States on Rough Surfaces"
Langmuir, **20**, 2004, 7097-7102.

[75] Nosonovsky, M. and Bhushan, B.
"Hierarchical roughness makes superhydrophobic states stable"
Microelectronic Engineering, **84**, 2007, 382-386.

[76] Gao, N. and Yan, Y.
"Modeling Superhydrophobic Contact Angles and Wetting Transition"
Journal of Bionic Engineering, **6**, 2009, 335-340.

[77] Whyman, G. and Bormashenko, E.
"How to Make the Cassie Wetting State Stable?"
Langmuir, **27**, 2011, 8171-8176.

[78] Bormashenko, E., Musin, A., Whyman, G., Zinigrad, M.
"Wetting Transitions and Depinning of the Triple Line"
Langmuir, **28**, 2012, 3460-3464.

[79] Zheng, Q.-S., Yu, Y., Zhao, Z.-H.
"Effects of Hydraulic Pressure on the Stability and Transition of Wetting Modes of Superhydrophobic Surfaces"
Langmuir, **21**, 2005, 12207-12212.

[80] Moulinet, S. and Bartolo, D.
"Life and death of a fakir droplet: Impalement transitions on superhydrophobic surfaces"
Eur. Phys. J. E, **24**, 2007, 251-260.

[81] Tuteja, A., Choi, W., Minglin, M., Mabry, J. M., Mazzella, S. A., Rutledge, G. C., McKinley, G. H., Cohen, R. E.
"Designing Superoleophobic Surfaces"
Science, **318**, 2007, 1618-1622.

[82] Tuteja, A., Choi, W., Mabry, J. M., McKinley, G. H., Cohen, R. E.
"Robust omniphobic surfaces"
PNAS, **105**, 2008, 18200-18205.

[83] Wang, J. and Chen, D.
"Criteria for Entrapped Gas under a Drop on an Ultrahydrophobic Surface"
Langmuir, **24**, 2008, 10174-10180.

[84] Afferrante, L. and Carbone, G.
"Microstructured superhydrorepellent surfaces: effect of drop pressure on fakir-state stability and apparent contact angles"
J. Phys.: Condens. Matter, **22**, 2010, 325107.

[85] Forsberg, P., Nikolajeff, F., Karlsson, M.
"Cassie-Wenzel and Wenzel-Cassie transitions on immersed superhydrophobic surfaces under hydrostatic pressure"
Soft Matter, **7**, 2011, 104-109.

[86] Patankar, N. A.
"Consolidation of Hydrophobic Transition Criteria by Using an Approximate Energy Minimization Approach"
Langmuir, **26(11)**, 2010, 8941-8945.

[87] Adamson, A. W. and Gast, A. P,
"Physical Chemistry of Surfaces"
John Wiley & Sons, Inc., 1997, pp. 6-8.

[88] Bormashenko, E., Bormashenko, Y., Whyman, G., Pogreb, R., Stanevsky, O.
"Micrometrically scaled textured metallic hydrophobic interfaces validate the Cassie-Baxter wetting hypothesis"
J. Colloid Interface Sci., **302**, 2006, 308-311.

[89] Bormashenko, E., Bormashenko, Y., Stein, T., Whyman, G., Pogreb, R.
"Environmental scanning electron microscopy study of the fine structure of the triple line and Cassie-Wenzel wetting transition for sessile drops deposited on rough polymer substrates"
Langmuir, **23**, 2007, 4378-4382.

[90] Holdgate, M. W.
"The Wetting of Insect Cuticles by Water"
Journal of Experimental Biology, **32(3)**, 1955, 591-617.

[91] Blow, M. L. and Yeomans, J. M.
"Superhydrophobicity on Hairy Surfaces"
Langmuir, **26(9)**, 2010, 16071-16083.

[92] Patankar, N. A.
"On the Modeling of Hydrophobic Contact Angles on Rough Surfaces"
Langmuir, **19**, 2003, 1249-1253.

[93] Fjellvang, K.
"Lessons from Nature, the Wetting of Springtail Cuticles"
Unpublished master's thesis, Norwegian University of Science and Technology, Trondheim, Norway, 2012.

[94] Lobaton, E. J. and Salamon, T. R.
"Computation of constant mean curvature surfaces: Application to the gas-liquid interface of a pressurized fluid on a superhydrophobic surface"
Journal of Colloid and Interface Science, **314**, 2007, 184-198.

[95] Adamson, A. W. and Gast, A. P,
"Physical Chemistry of Surfaces"
John Wiley & Sons, Inc., 1997, pp. 35-40.

[96] Nearing, M. A., Bradford, J. M., Holtz, R. D.
"Measurement of Waterdrop Impact Pressures on Soil Surfaces"
Soil Sci. Soc. Am. J., **51**, 1987, 1302-1306.

[97] Dorrer, C. and Rühe, J.
"Micro to nano: Surface size scale and superhydrophobicity"
Beilstein J. Nanotechnol., **2**, 2011, 327-332.

[98] Dufour, R., Brunet, P., Harnois, M., Boukherroub, R., Thomy, V., Senez, V.
"Zipping Effect on Omniphobic Surfaces for Controlled Deposition of Minute Amounts of Fluid or Colloids"
Small, **8**, 2012, 1229-1236.

[99] Öner, D. and McCarthy, T. J.
"Ultrahydrophobic Surfaces. Effects of Topography Length Scales on Wettability"
Langmuir, **16**, 2000, 7777-7782.

[100] Teisala, H., Tuominen, M., Aromaa, M., Stepien, M., Mäkelä, J. M., Saarinen, J. J., Toivakka, M., Kuusipalo, J.
"Nanostructures Increase Water Droplet Adhesion on Hierarchically Rough Superhydrophobic Surfaces"
Langmuir, **28**, 2012, 3138-3145.

[101] Feng, L., Zhang, Y., Xi, J., Zhu, Y., Xia, F., Jiang, L.
"Petal Effect: A Superhydrophobic State with High Adhesive Force"
Langmuir, **24**, 2008, 4114-4119.

[102] Teisala, H., Tuominen, M., Kuusipalo, J.
"Adhesion Mechanism of Water Droplets on Hierarchically Rough Superhydropho-

bic Rose Petal Surface"
Journal of Nanomaterials, 2011, Article ID 818707, 6 pages.

A. Springtail cuticle images

Images used to extract surface parameters required for the calculations above are collected in this section. These comprise SEM and AFM images characterizing the cuticle of nine different springtail species, as well as the TEM image presented in Figure 3 (the images in Figures 2 and 3 are repeated here for completeness). The images of higher magnification highlight the cuticle pattern on the dorsal part of the springtail bodies (their 'backs').

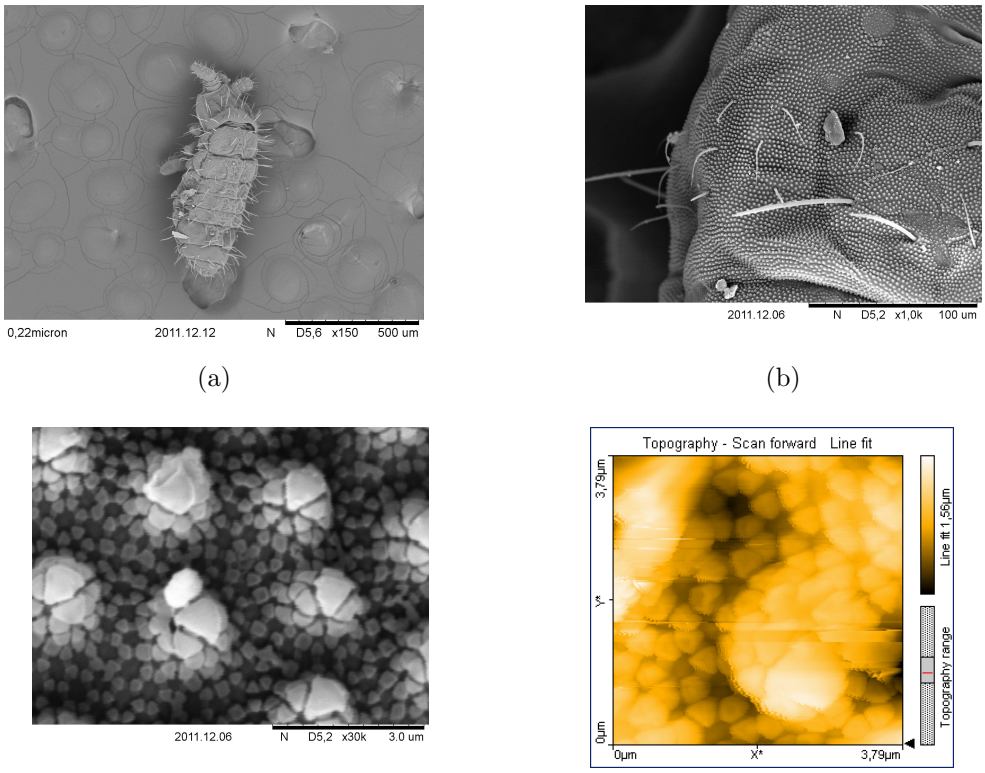

(a) (b)

(c) (d)

Figure 20: *Hypogastura viatica*

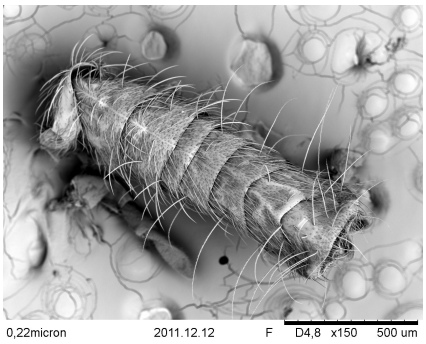

(a)

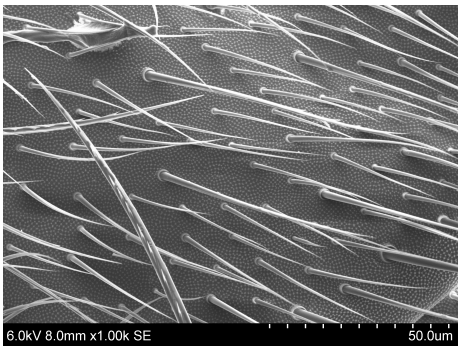

(b)

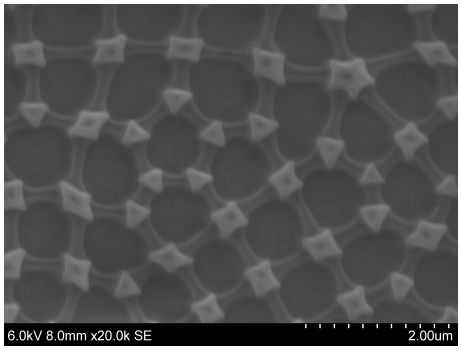

(c)

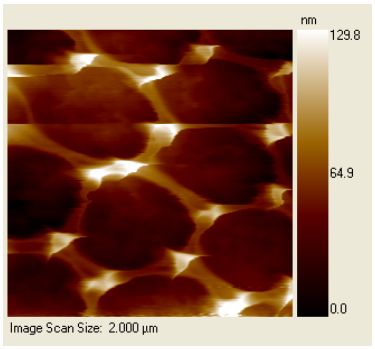

(d)

Figure 21: *Isotomurus prasis*

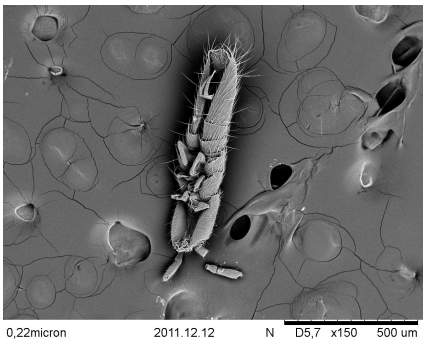

(a)

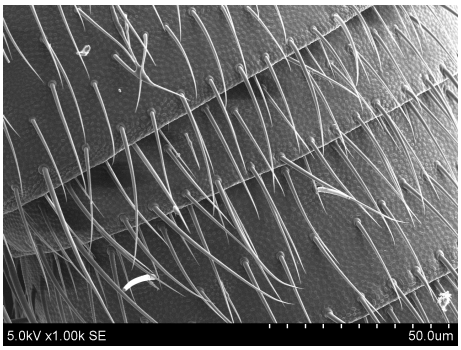

(b)

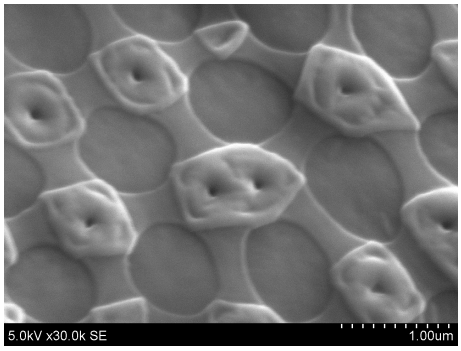

(c)

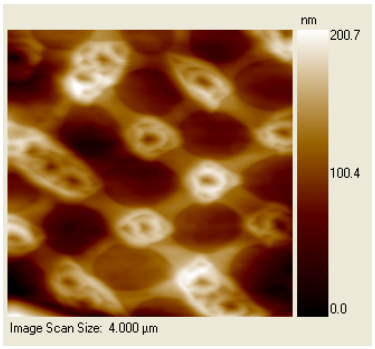

(d)

Figure 22: *Folsomia quadrioculata*

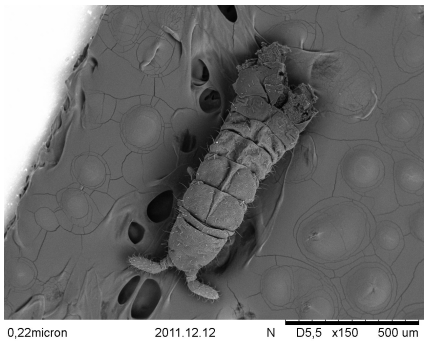

(a)

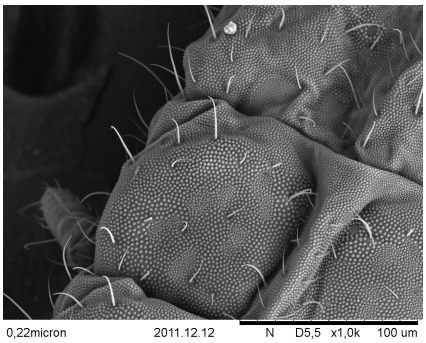

(b)

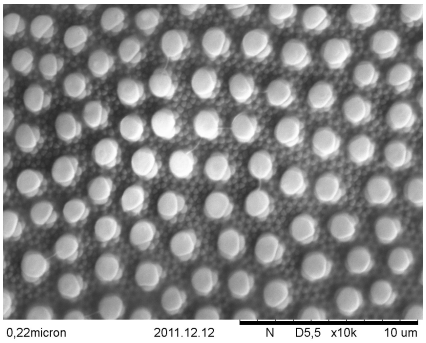

(c)

Figure 23: *Anurophorus septentrionalis*

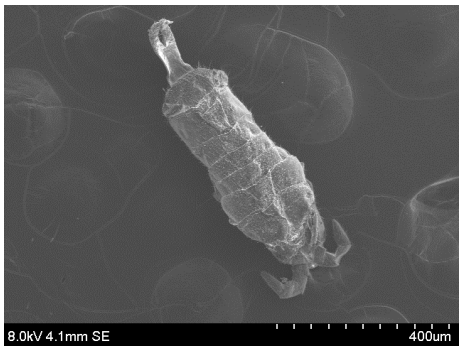

(a)

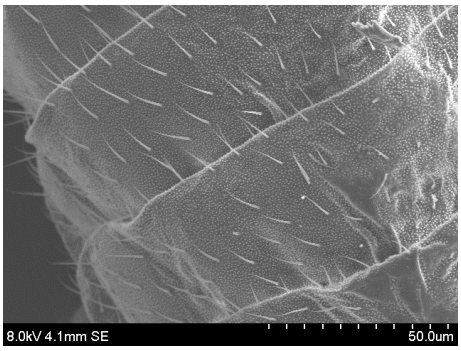

(b)

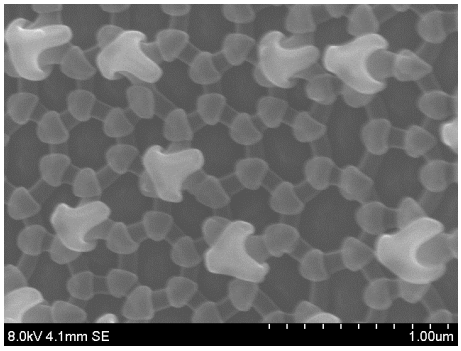

(c)

Figure 24: *Archisotoma besellsi*

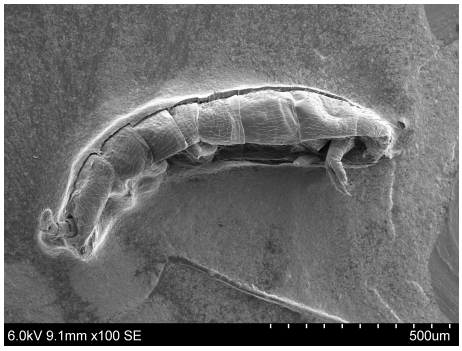

(a)

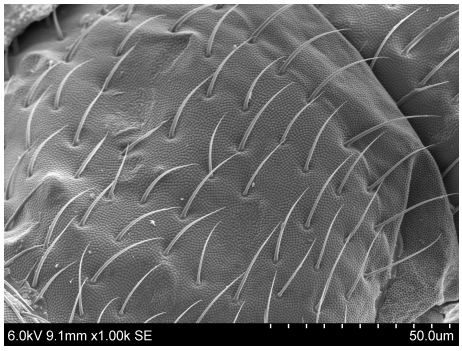

(b)

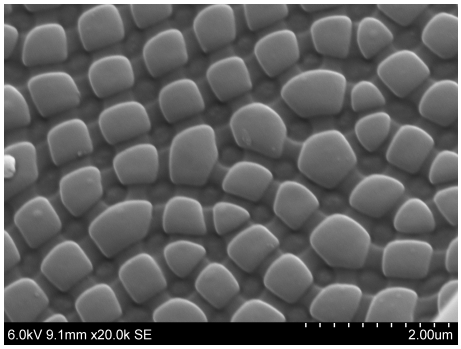

(c)

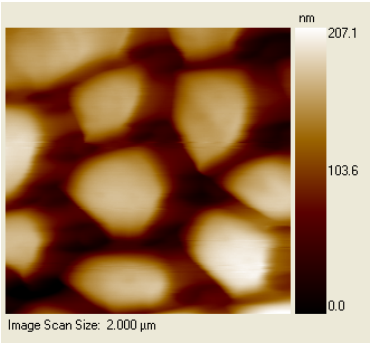

(d)

Figure 25: *Cryptopygus clavatus*

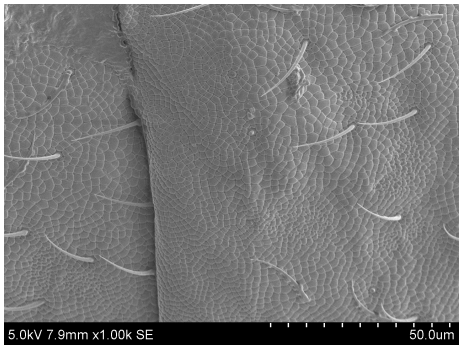

(a)

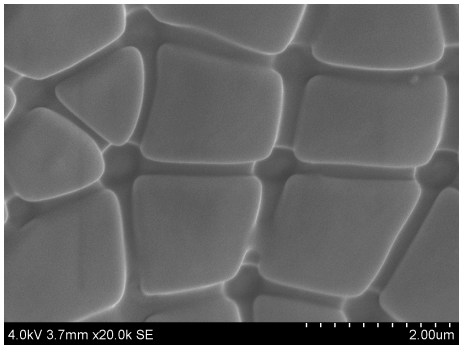

(b)

Figure 26: *Anurophorus laricis*

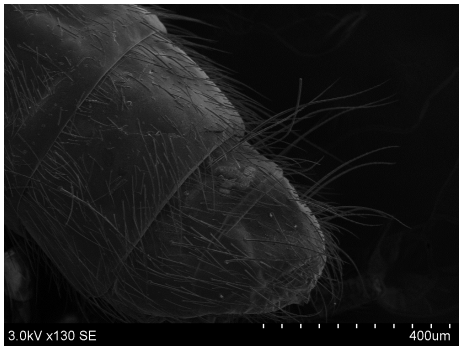

(a)

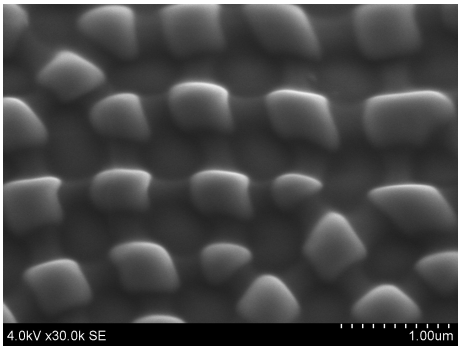

(b)

Figure 27: *Isotoma anglicana*

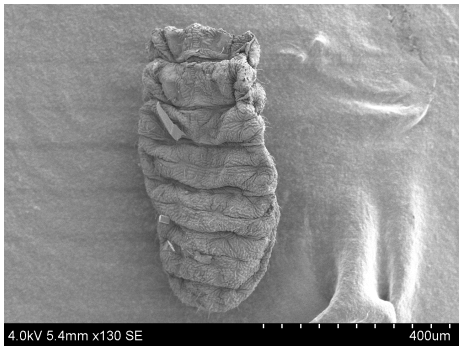

(a)

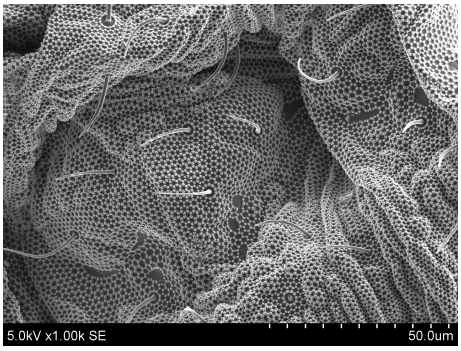

(b)

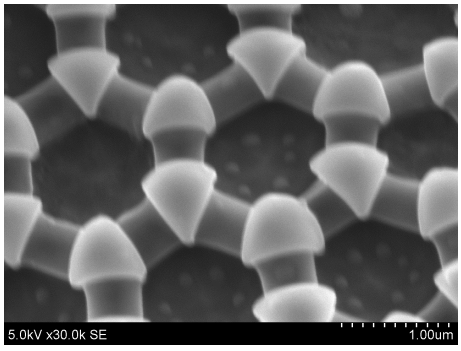

(c)

Figure 28: *Xenilla maritima*

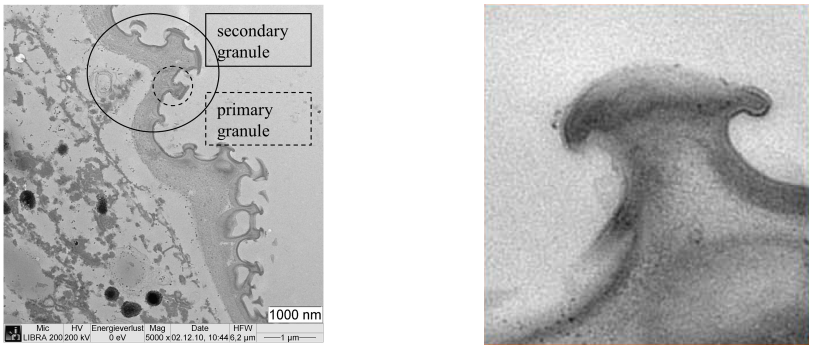

(a) (b)

Figure 29: (a) TEM image of a cuticle cross-section of the springtail species *Ceratophysella denticulata* [19]. (b) Magnified view of one of the primary granules present in (a), demonstrating an overhanging granule profile.